Dissecting the subcellular forces sculpting early *C. elegans* embryos

Kazunori Yamamoto[1,2*], Sacha Ichbiah[3*], Joana Pinto[4], Fabrice Delbary[3], Nate Goehring[4], Hervé Turlier[3†], Guillaume Charras[1,5,6†]

[1] London Centre for Nanotechnology, University College London, 17-19 Gordon Street, London WC1H 0AH, UK
[2] Applied Bioscience, Kanagawa Institute of Technology, 1030 Shimo-Ogino Atsugi Kanagawa, 243-0203, Japan
[3] Center for Interdisciplinary Research in Biology (CIRB), Collège de France, CNRS, INSERM, Université PSL, 11, place Marcelin Berthelot, Paris, 75005, France
[4] The Francis Crick Institute, London NW1 1AT, UK
[5] Department of Cell and Developmental Biology, University College London, Gower Street, London WC1E 6BT, UK
[6] Institute for the Physics of Living Systems, University College London, Gower Street, London WC1E 6BT, UK

* These authors contributed equally to this work

† Corresponding authors: herve.turlier@college-de-france.fr, g.charras@ucl.ac.uk

Summary

Embryo shape is governed by the mechanics of individual cells, the strength of intercellular interactions, and geometrical constraints. Models in which cells interact through surface tensions successfully predict cell arrangement within aggregates. However, predicting cell shape dynamics remains challenging because of difficulties in measuring temporal changes in tensions. Here, we dissect the spatiotemporal changes in cellular surface tensions that sculpt the early nematode embryo, using AFM measurements and inverse modeling. We validate a hybrid tension inference pipeline that combines dynamic information from cell geometry and cortical myosin enrichment. The inferred spatiotemporal tensions allow prediction of morphogenesis in wild-type embryos as well as phenotypic changes arising from protein depletion. We further uncover a direct and non-affine contribution of cadherins to cell contact tensions, whose magnitude is comparable to cadherins' indirect contribution via actomyosin regulation. Overall, our inference pipeline allows characterization of the forces underlying morphogenesis and their relationship to molecular processes.

Keywords

C. elegans embryo, cortical tension, tension inference, cadherin, myosin, active-foam simulation

Highlights

- P lineage cells have lower cortical tensions than AB lineage cells
- The balance between cortical and cell-cell interfacial tensions determines, together with the confinement within the eggshell, the shape of the *C. elegans* embryo.
- Abundance of Myosin-II is a good predictor of cortical tension but is not sufficient to determine

tension at cell-cell contacts.

- Myosin-informed tension inference allows determination of the spatiotemporal evolution of all surface tensions within the embryo.
- Cadherins contribute non-linearly to tension at cell-cell contacts.

Open Access

For the purpose of Open Access, the author has applied a CC BY public copyright license to any Author Accepted Manuscript version arising from this submission.

Introduction

The shape of embryos is governed by the mechanics of its constituent cells, the strength of their intercellular interactions, and geometric constraints. During development, cells continuously alter their mechanical properties and modulate their interactions as they undergo differentiation in response to spatiotemporal developmental cues. The combination of many individual cellular mechanical changes drives tissue morphogenesis. Over the past decade, our understanding of the forces shaping embryos has progressed rapidly. Many studies have examined later stages of development involving large numbers of – generally epithelial – cells, such as convergence and extension or gastrulation (Behrndt et al., 2012; Collinet et al., 2015; Firmino et al., 2016; Munro and Odell, 2002; Tada and Kai, 2012; Voiculescu et al., 2007). Others have investigated earlier developmental stages in which groups of cells undergo slow uniform changes in mechanics (Maitre et al., 2016; Sherrard et al., 2010). In all cases, the dynamics of mechanical changes were sufficiently slow to ensure a quasi-static evolution of mechanics. Surprisingly, *C. elegans* morphogenesis has received little attention, despite its wide-spread use as a model system for genetics and development. Compared to other model systems, such as mouse (Maitre et al., 2016) and human preimplantation embryos (Firmin et al., 2022), drosophila retina (Godard et al., 2020; Hayashi and Carthew, 2004), ascidians (Godard et al., 2020) or frog gastrula (David et al., 2014)), the development and lineage specification in the *C. elegans* embryo is very rapid. At early stages, the cell cycle lasts only 10-20 minutes and cell type is specified from the 4-cell stage onwards by a combination of asymmetric divisions, rotational movements (Singh and Pohl, 2014; Sugioka and Bowerman, 2018), as well as Wnt (Rocheleau et al.) and Notch signaling (Mickey et al., 1996; Thorpe et al., 1997). Those processes are tightly controlled, ensuring an invariant development with small embryo to embryo morphogenetic variations. Thus, nematode embryos present a true challenge for cell morphogenetic characterization, being fast developing with early cell lineage specification.

Predicting embryo shape dynamics from the mechanical changes occurring in each of its cells remains a second challenge. This is partly due to the difficulty of exhaustively characterizing the mechanics of each individual cell surface within embryos. Mechanical characterization methods require direct contact with the cell to be probed, such as micropipette aspiration (Guevorkian and Maitre, 2017; Mitchison and Swann, 1954) or atomic force microscopy (AFM) (Barriga et al., 2018), making them unsuitable for embryos contained within a cuticle or for cells deep within aggregates. Other methods, such as laser ablation (Rauzi et al., 2008), ferrofluid droplets (Serwane et al., 2017) or optical tweezers (Bambardekar et al., 2015), can sample mechanical properties within embryos but only sparsely in time or space. Brillouin microscopy shows great promise but translating its output into mechanical properties suitable for modeling and simulations remains unachieved (Prevedel et al., 2019). As a

result, alternative approaches have been developed recently to infer mechanics from image data of cell membranes. These methods assume that embryos can be treated as heterogeneous foams in which cells interact through their surface tensions (Brodland et al., 2010). Such assumptions allow to deduce the relative surface tension in all interfaces from the geometry of cells but determining temporal changes from time-lapse microscopy of morphogenesis remains challenging. Recent inference methods applied to epithelial tissues showed that surface tensions correlate with the molecular composition at cell contacts (e.g. myosin enrichment) (Brodland et al., 2010; Chan et al., 2017; Kale et al., 2018; Noll et al., 2020). Yet, none of these methods used temporal measurements of molecular changes to connect inferred force maps in time, nor have they been validated via direct tension measurements or in cell aggregates with more complex three-dimensional shapes such as early embryos.

While much is known about signaling and cell fate specification in the early *C. elegans* embryo, our knowledge of the cellular mechanical changes underlying its morphogenesis remain scarce. In many organisms, changes in cell shape and embryo morphology appear mostly regulated by differences in myosin enrichment at cell interfaces. This is the case for example in the 8-cell stage mouse embryo, where myosin levels increase at cell-medium surfaces and decrease at cell-cell interfaces, driving embryo compaction (Maitre et al., 2016). Similar roles of myosin in cell arrangement are likely in *C. elegans* as early divisions result in asymmetric segregation of myosins across daughter cells (Mayer et al., 2010; Munro et al., 2004). The role of cell adhesion proteins, such as cadherins, remains less well understood and their partitioning is not well characterized. In principle, binding of adhesion proteins across cell-cell interfaces could directly decrease interfacial tension. However, in most organisms (such as mouse and zebrafish), this direct contribution is negligible compared to cadherin's indirect contribution, which results from a decrease in myosin activity via downregulation of RhoA downstream of recruitment of p120-catenin by the cadherin cytoplasmic domain (Yu et al., 2016). In other model systems, such as Drosophila, cadherins appear to have a weak direct contribution and a more substantial indirect contribution (Chan et al., 2017). Thus, the relative importance of motor activity and intercellular adhesion remains poorly understood in the control of surface tension at intercellular contacts and cell arrangement in tissues and embryos.

Here, we dissect the spatiotemporal changes in cellular surface tensions that sculpt the early nematode embryo. For this, we developed a hybrid tension inference pipeline that combines dynamic information from cell geometry and cortical myosin fluorescence. After validating it with AFM, we determined the spatiotemporal forces shaping the early *C. elegans* embryo and showed with 3D active-foam simulations that these are sufficient to predict shape changes in wild-type embryos as well as phenotypic changes arising in embryos subjected to proteins depletion. Finally, our methods reveal a

direct and non-affine contribution of cadherins to cell-cell interfacial tensions, whose magnitude is comparable to cadherin's indirect contribution via actomyosin depletion and must be included to predict cell arrangements accurately.

Results

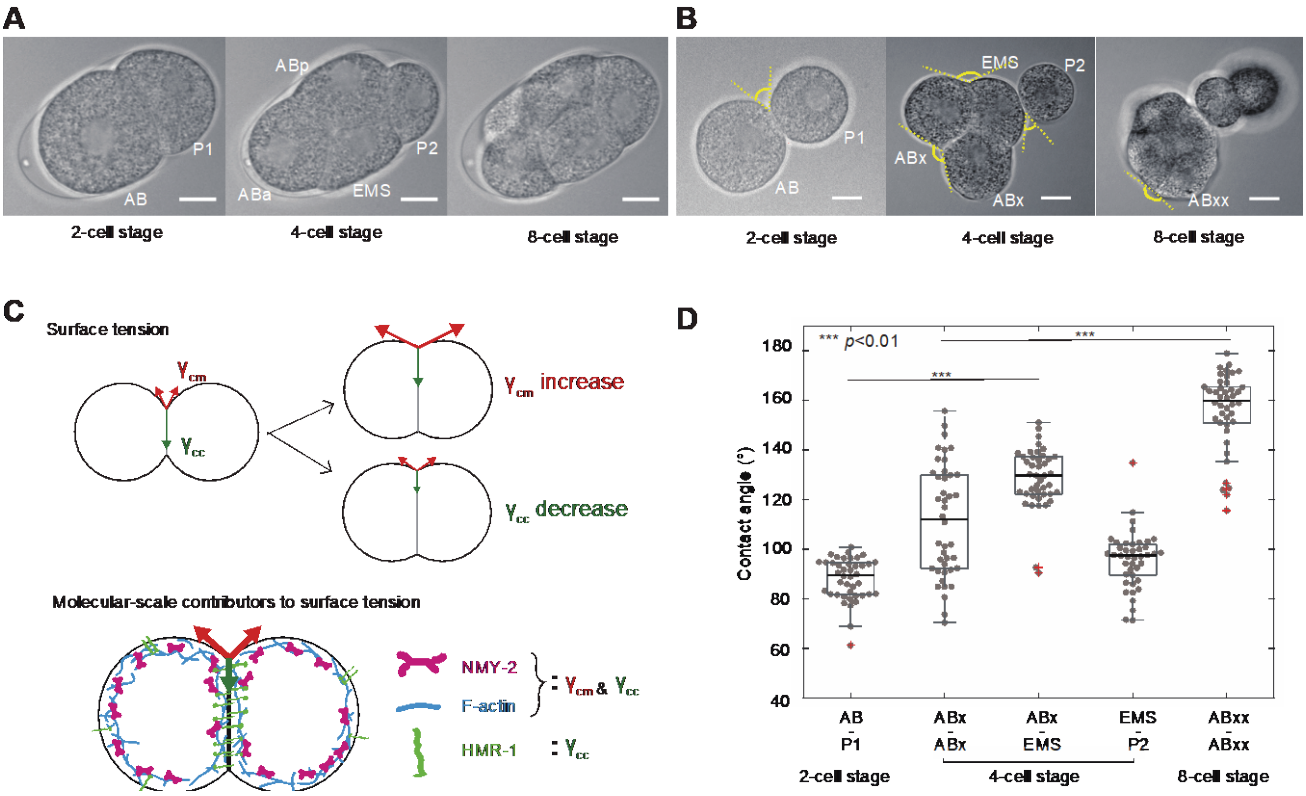

Figure 1: The early *C. elegans* embryo undergoes cell-specific mechanical changes

A. Brightfield images of *C. elegans* embryos at the 2-, 4-, and 8-cell stages. Scale bars=10 µm. **B**. Brightfield images of *C. elegans* embryos with the eggshell removed at the 2-, 4- and 8-cell stage. Cell names appear next to each cell in the 2- and 4-cell stage images. Dashed yellow lines display the external angle of contact between cells. Scale bars=10 µm. **C**. Top: The external angle of contact between two cells depends on the balance of cortical tension γ_{cm} in each cell (red arrows) and the interfacial tension γ_{cc} at the intercellular contact (green arrow). If the angle of contact increases, this can be due to an increase in γ_{cm}, a decrease in γ_{cc}, or a combination of both. Bottom: At the molecular-scale, the cortical tension γ_{cm} arises from the action of myosin motor proteins (NMY-2, magenta) on the F-actin scaffold (blue). In addition to these proteins, the interfacial tension γ_{cc} also involves direct and indirect contributions from cell-cell adhesion proteins (E-cadherin or HMR-1, green) and their interactors. **D.** Contact angles measured from brightfield images at different stages of embryonic development in embryos without eggshells. Boxplots indicate the 25th and 75th percentiles, the black line within the box indicates the median, and the whiskers extend to the most extreme data points that are not outliers. Outliers are indicated by red crosses. Individual data points are indicated by grey dots.

Early *C. elegans* development involves dynamic, cell- and stage-specific changes in mechanics

Despite its small number of cells, the early *C. elegans* embryo acquires complex shapes that point to mechanical heterogeneity of the cells (**Fig 1A**). The one cell embryo first undergoes an asymmetric division to give rise to AB and P_1. AB then divides symmetrically into ABa and ABp, which are identified based on their position within the embryo; whereas P_1 divides asymmetrically into EMS and P_2. Together, ABa, ABp, and EMS form a compact aggregate, with P_2 bulging out from this group (**Fig 1A, S1A**, 4-cell stage normalized time=0.1). Further divisions beyond the 4-cell stage give rise to complex non-planar 3D packing of the cells within the embryo but clear differences in contact angles between cells can nevertheless be observed. Overall, these observations imply dynamic and cell-specific regulation of mechanics within the embryo.

To gain a qualitative understanding into the forces shaping the early *C. elegans* embryo, we first examined the contact angles between cells. Indeed, the external contact angle θ between two neighboring cells is controlled by the balance of tensions in the cortex of each cell γ_{cm1} and γ_{cm2} and the tension at their intercellular contact γ_{cc} (**Fig 1C**). Any change in the angle of contact results from a change in cell mechanics. For example, if the contact angle θ increases, this could be because γ_{cm} increases in one or both of the cells, because γ_{cc} decreases, or because of a combination of both (Turlier and Maitre, 2015).

During its development, the *C. elegans* embryo is confined in a protective eggshell shaped as a prolate ellipsoid (**Supplemental theory Fig 4A**). As confinement may influence surface tensions, we removed the embryos from their eggshell at the 1- or 2-cell stage to measure angles of contact between cells in brightfield images. This revealed very clear differences in how cells contacted one another (**Fig 1B, S1B**). Outside of the eggshell, the positional information that allows to distinguish ABa and ABp is lost and we therefore designate these cells as ABx and their daughters as ABxx. At the 4-cell stage, EMS and the two ABx cells formed a compact aggregate with P_2 appearing weakly bound to EMS. Later, ABxx cells formed a compact aggregate with MS, and E, P3 and C remained weakly attached to this group. From a morphological standpoint, cells located at the anterior of the embryo ABx(2)-EMS and ABxx(4)-MS appeared to form increasingly compact clusters of cells, similar to what is observed in 8-cell mouse embryos (Maitre et al., 2015). These qualitative relationships were also reflected in the angles of contact between cells. The angle of contact between cells of the P and the AB lineages increased between the 2- and 4-cell stage (**Fig 1D**). Similarly, the angle of contact between ABxx cells was larger than between ABx cells (**Fig 1D**). Overall, the changes in contact angle and embryo morphology indicated that cells within the embryos possess clear mechanical differences and that their mechanics evolves even during the earliest stages of morphogenesis.

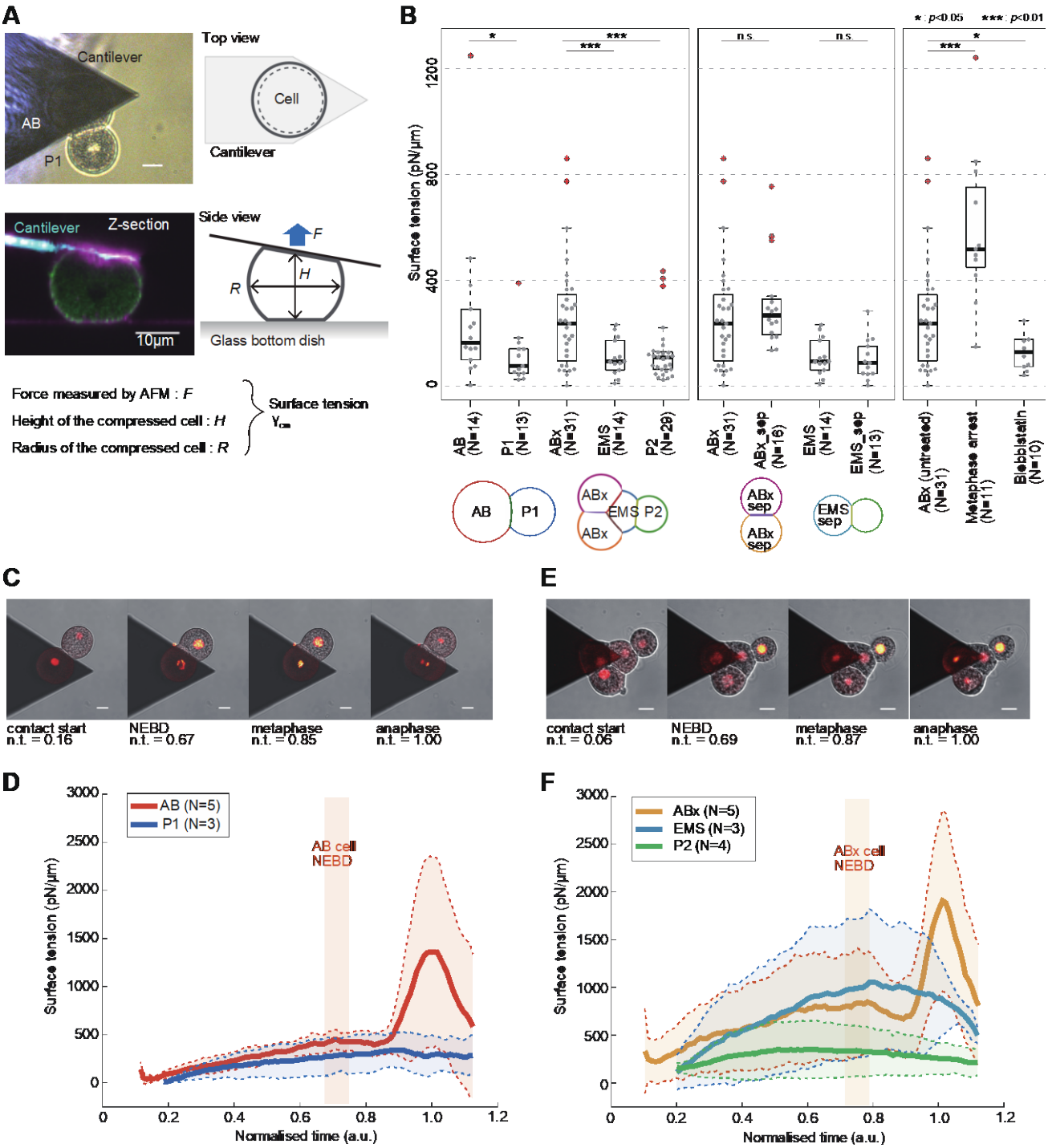

Figure 2: AB and P lineage cells are mechanically different in 2- and 4-cell stage *C. elegans* embryos

A. *C. elegans* embryos during AFM measurements of cortical tension. Top left: brightfield image of an AFM cantilever in contact with the AB cell in a 2-cell stage embryo. Scale bar= 10µm. Top right: schematic diagram of the measurement. Bottom left: profile view of the AFM cantilever in contact with the AB cell of a 2-cell stage embryo. The cell membrane is labelled with CellMask (magenta) and the embryo expresses NMY-2::GFP (green). The AFM cantilever is visualized by reflection (cyan). Bottom right: diagram indicating the force exerted by the embryo on the AFM cantilever (blue arrow)

and the cell dimensions (black double arrow). **B.** Single time point measurements of cortical tension in cells of the *C. elegans* embryo at the 2- and 4-cell stages. Boxplots indicate the 25th and 75th percentiles, the thick black line indicates the median, and the whiskers extend to the most extreme data points that are not outliers. Outliers are indicated by red crosses. Individual data points are indicated by grey dots. Left: Cortical tension in the cells of the embryo at the 2- and 4-cell stages. A diagram of the cellular arrangement in those stages is presented below the graph. Middle: Comparison of the cortical tension in cells from intact embryos and from embryos in which AB and P_1 were separated. After cell division, tension is measured in the ABx cell (ABx-sep) and in the EMS cell (EMS-sep). Right: Cortical tensions in ABx cells in untreated embryos and in embryos treated with blebbistatin to inhibit myosin contractility or arrested in metaphase by proteasome inhibition with c-lactocystin-ß-lactone. The number of measurements in each condition is indicated on the x-axis. **C.** Time series of a 2-cell embryo during cortical tension measurement. The cantilever is visible as a triangular dark shadow and is in contact with the AB cell. The GFP:: H2B signal is overlaid on the brightfield microscopy images in red, allowing determination of the phase of the cell cycle. **D.** Temporal evolution of cortical tension in the AB cell (average of n=5 embryos) and the P_1 cell (n=3 embryos). The solid line indicates the mean and the shaded area the standard deviation. Time was normalized to the cell cycle. **E.** Time series of a 4-cell embryo during cortical tension measurement. The cantilever is visible as a triangular dark shadow and is in contact with an ABx cell. The GFP::H2B signal is overlaid on the brightfield microscopy images in red to allow determination of the phase of the cell cycle. **F.** Temporal evolution of cortical tension in the ABx cell (average of n=5 embryos), the EMS cell (n=3 embryos) and the P_2 cell (n=4 embryos). The solid line indicates the mean and the shaded area the standard deviation. Time was normalized to the cell cycle.

Cortical tension differs across cell lineages

To directly probe mechanical differences in 2- and 4-cell stage embryos, we measured the cortical tension γ_{cm} in each individual cell using Atomic Force Microscopy (AFM) (**see star methods and SI, Fig 2, Fig S1E-G**). As these measurements require direct contact between a microfabricated cantilever and the cell, we removed the embryonic eggshell. AFM-based tension measurements are usually carried out on isolated cells but, as a first step, we assumed that the presence of a cell-cell contact on part of the cell periphery did not significantly affect estimation of cortical tension. In our experiments, we brought a tipless AFM cantilever into contact with a cell and waited 30s for the measured force to relax to a plateau (**Fig S1E**) (Fischer-Friedrich et al., 2014). This allowed passive stresses originating from deformation of the cortical F-actin network to be dissipated by turnover and ensured that we measured only steady-state tension arising from active mechanisms, such as myosin contractility (Fischer-Friedrich et al., 2014). The force at the plateau together with the geometry of the cell allow to estimate the cortical tension by solving the Laplace equation along the lateral cell profile (Norotte et al., 2008) (**see Methods and Supplemental theory**).

Cortical tension in *C. elegans* cells ranged between 50-350 pN/µm (**Fig 2B**), comparable to that

reported in interphase in mammalian cultured and embryonic cells (Chugh et al., 2017; Maitre et al., 2016) as well as in invertebrate embryos (Godard et al., 2020). Interestingly, clear mechanical differences were evident between cell lineages. Cells of the AB lineage (AB and ABx) had tensions ~3-fold larger than the P lineage cells (P_1, P_2) (**Fig 2B**). However, within a lineage, the cortical tension between mother and daughter cells did not appear significantly different (**Fig 2B, left**). To determine if the presence of intercellular contacts affects cortical tension estimation, we separated P_1 from AB at the 2-cell stage, waited for each of these cells to divide, and measured the cortical tension in ABx_{sep} and EMS_{sep}. We found no significant difference in cortical tension between ABx, which has 2 contacts, and ABx_{sep}, which has only one, or between EMS, which has 3 contacts, and EMS_{sep}, that only has one (**Fig 2B, middle**). This suggests that the presence of contacts has a less significant effect on cell-medium cortical tension estimation than other sources of experimental noise.

One likely reason for the observed mechanical differences between the AB and P lineages is the asymmetric partitioning of actomyosin that takes place during the first cell division (Mayer et al., 2010; Munro et al., 2004). Indeed, in many model systems, the submembranous actomyosin cortex is a key determinant of cell surface tension (Maitre et al., 2015; Salbreux et al., 2012). When we imaged the actomyosin content in 4-cell stage embryos, we could observe clear differences in myosin intensity with ABa and ABp being brighter than EMS and P_2 (**Fig S2A**), whereas differences in F-actin staining were more subtle (**Fig S2A-B**). This suggested that, as in other model systems, myosin may play a key role in setting cellular mechanical properties. Consistent with this, inhibition of myosin contractility with blebbistatin decreased cortical tension in ABx cells and, conversely, metaphase arrested cells, in which myosin activity is upregulated, displayed increased cortical tension (**Fig 2B, right**). Together, these experiments reveal clear differences in cortical tension between cells in the embryo that result from asymmetric partitioning of myosin over successive divisions.

Cortical tension evolves dynamically during the cell cycle

In our single time-point measurements (**Fig 2B**), we observed a large spread in cortical tensions. As there was a clear increase in cortical tension in metaphase, we hypothesized that the spread might arise because the cortical tension γ_{cm} evolves dynamically during the cell cycle and our measurements took place at different times in this cycle.

To determine temporal changes in cortical tension, we brought the AFM cantilever into contact with one of the cells of the embryo and allowed the force to relax. Then, we kept the cantilever in contact with the cell and monitored temporal changes in restoring force. If the cell geometry does not change, temporal variations in force reflect temporal changes in the surface tension γ_{cm} due to active

processes - such as changes in cortical myosin activity or enrichment. Simultaneously, we imaged GFP::H2B localization to follow cell cycle progression (**Fig 2C, E**). Cortical tension increased dynamically during interphase in all cells (**Fig 2D, F and Fig S1F, G**). At the 2-cell stage, γ_{cm}^{AB} increased ~3-fold over the course of interphase, reaching a maximum at Nuclear Envelope Breakdown (NEBD) (red line, **Fig 2D, Fig S1F**). In anaphase, the force applied on the cantilever increased dramatically due to a change in geometry because the AB cell often divided perpendicular to the plane of the coverslip. γ_{cm}^{P1} was systematically lower than γ_{cm}^{AB} but it also increased ~3-fold (blue line, **Fig 2D, Fig S1F**). No large change in force was observed at anaphase in P_1 because it always divided in the plane. At the 4-cell stage, the ABx cells displayed a ~2-fold increase in tension (orange line, **Fig 2F**). γ_{cm}^{EMS} was initially 3-fold smaller than γ_{cm}^{ABx} at the beginning of its cell cycle but increased over 4-fold, reaching a value comparable to γ_{cm}^{ABx} by NEBD (light blue line, **Fig 2F, Fig S1G**). This dramatic change in cortical tension may play a key role in the compaction of ABx(2)-EMS observed at the end of the 4-cell stage (**Fig 1A,B**). In contrast, γ_{cm}^{P2} remained the lowest and only increased by ~50% during the cell cycle (green line, **Fig 2F, Fig S1G**).

Overall, our data show that large dynamic increases in cortical tension take place during the cell cycle and suggest that these may drive the compaction of ABa, ABp, and EMS in the anterior of the embryo.

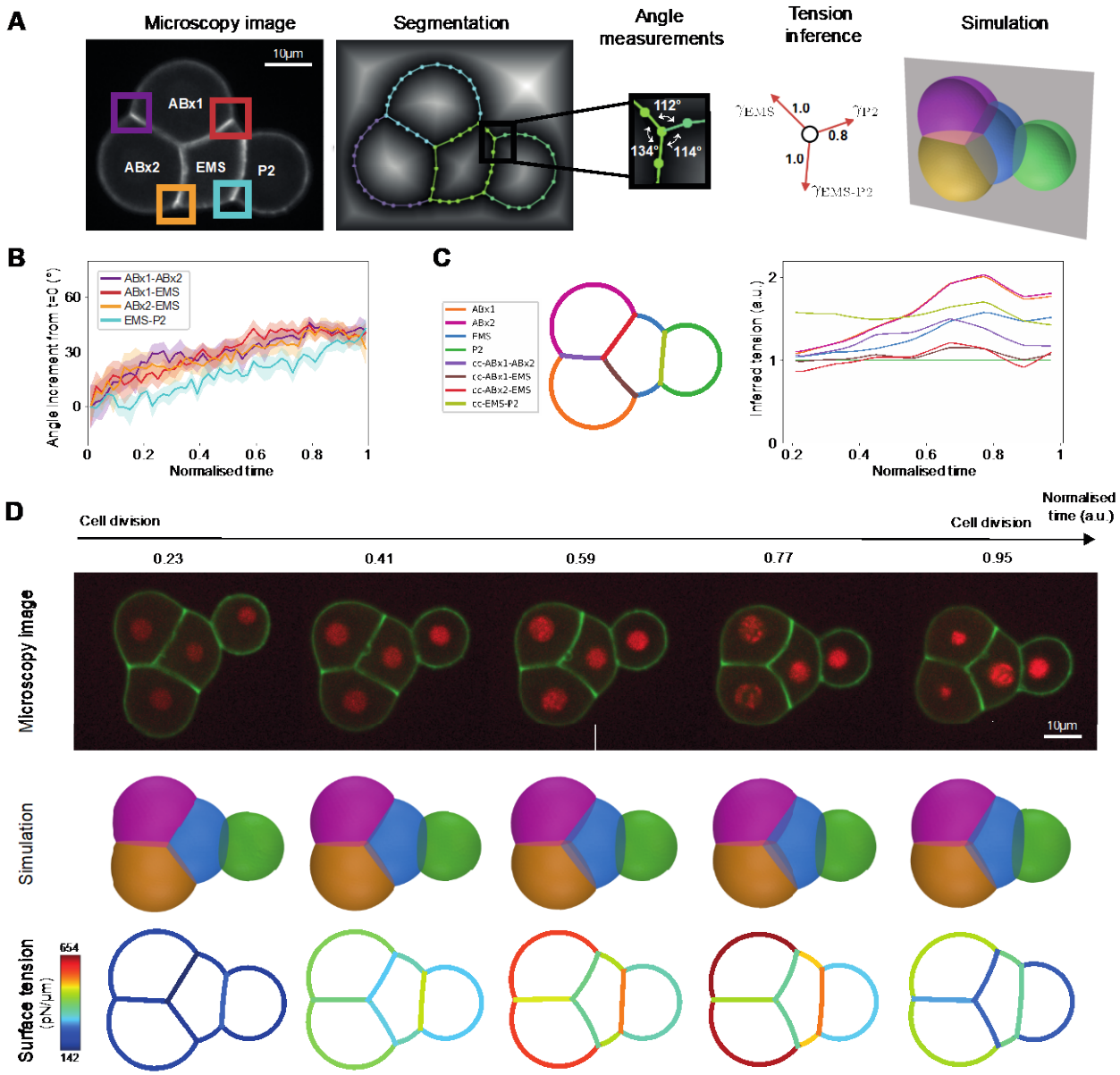

Fig 3: Tension inference allows prediction of spatiotemporal shape changes in the embryo

A. Tension inference pipeline. Microscopy images of the cell membrane (first column) are segmented and the cell outlines are represented by polygonal lines (second column). At each contact point where three cell surfaces meet, the angles between all surfaces are determined (third column). The relative tensions in each surface are then inferred based on the angles of contact (fourth column). 3D computational simulations predict cell arrangement (fifth column) based on the relative tensions in each surface. **B.** Temporal evolution of the change in angles of contact at tricellular junctions. Time is normalized to the cell cycle. **C.** Temporal evolution of inferred surface tensions relative to P_2. Color code is indicated on the left. **D.** Temporal evolution of inferred tension allows prediction of the cell arrangement in embryos. First row: microscopy time series of a developing embryo outside of the eggshell. The membrane is visualized with GFP-PH-PLCδ

(green) and the histones are visualized with mCherry::his-58 (red). Scale bar=10µm. Second row: temporal evolution of predicted embryo shape. ABx1 appears in yellow, ABx2 in pink, EMS in blue, and P_2 in green. Third row: temporal changes in surface tension in pN/µm. The tension in each surface is color coded with dark blue representing low tension and red high tension.

Time-lapse imaging of cell membranes allows inference of surface tensions maps in the embryo

One key limitation of AFM measurements is that they necessitate direct contact between the cantilever and the cell of interest. This signifies that they can only be carried out in non-physiological conditions when the embryo has been removed from its eggshell. Furthermore, they do not allow to measure interfacial tensions at cell-cell contacts. As an alternative, we explored the use of tension inference (Roffay et al., 2021), which allows determination of surface tensions based on the angles of contact between cells.

In our experiments, we used a worm line that expresses a GFP-tagged membrane marker to allow segmentation of cell outlines (the PH domain of PLCδ) and an mCherry-tagged histone marker to allow determination of the cell cycle stage (**Fig 3A, left** and **Fig 3D**). Following segmentation (**Methods and Supplemental theory**), angles between membranes at each trisurface junctions were measured automatically (**Fig 3A, middle**). At these points, the three surface tensions must balance. As an alternative to the classical Young-Dupré relation, which relates contact tensions with cosines of the contact angles, we derived another equivalent expression for the balance of tensions between three surfaces (see **Supplemental theory Fig 3**). Denoting the three regions meeting at a trisurface junction by the indices i, j, k, this equation relates directly the value of each tension γ_{ij} at the interface between two regions i and j to the contact angles $\theta_{i,j,k}$ as follows: $\gamma_{ij} = \frac{t}{2}\cot\left(\frac{\theta_k}{2}\right)\left[\cot\left(\frac{\theta_i}{2}\right) + \cot\left(\frac{\theta_j}{2}\right)\right]$, where $t = \gamma_{ij} + \gamma_{jk} + \gamma_{ki}$ (see derivation in **Supplemental theory**). Knowledge of the angles at each trisurface junction within the embryo then forms a complete set of linear equations relating all tensions within the embryo. When complemented by an additional constraint to set a reference tension, this linear system is overdetermined and can be solved in a least-square sense using a Moore-Penrose pseudo-inverse (**Supplemental theory**). This allows inference of all surface tensions relative to a reference tension within the embryo, that we chose as P_1 for 2-cell stage embryos and P_2 for 4-cell stage embryos.

To account for differences in developmental time across embryos, we normalized time choosing the moment of closure of the cytokinetic ring of the mother cell as time 0 and the beginning of furrowing

in the next cell cycle as time 1 (**Fig S1A,B**). To allow comparison of angular change between different cell contacts, we plotted the change in angle relative to time 0 (**Fig 3B**). At the 4-cell stage, all angles of contact grew by ~40°, although their temporal dynamics were somewhat different. $\theta_{ABx1-ABx2}$ and $\theta_{ABxi-EMS}$ increased rapidly at the beginning of their cell cycle before slowing at NEBD. θ_{EMS-P2} grew at a lower but constant rate throughout the cell cycle. These data confirmed that dynamic changes in mechanics took place in all cells of the embryo.

Next, we inferred relative surface tension maps within the embryos without eggshells based on contact angle measurements. We chose the cortical tension in P_2 as reference because its absolute value varies little over time (**Fig 2F**), allowing us to estimate an approximate temporal evolution of surface tensions. With these assumptions, tension in the cortex of the ABx cells and EMS increased steadily, roughly doubling by t=0.8 when NEBD occurred (**Fig 3C**), broadly consistent with our AFM measurements (**Fig 2F**). In contrast, tensions at cell-cell contacts varied much less (**Fig 3C**). Interestingly, interfacial tension was specific to each contact with γ_{EMS-P2} being the largest, followed by $\gamma_{ABx-ABx}$, and finally $\gamma_{EMS-ABxi}$ (**Fig 3C**).

As a validation of tension inference for characterizing embryo mechanics, we predicted embryo shapes over the normalized cell cycle using inferred surface tensions and measured cell volumes (Fickentscher et al., 2018) as inputs to previously developed 3D active-foam simulations (Maitre et al., 2015). These predict the equilibrium cell shape and arrangement by minimizing a surface energy $E = \sum_{\{ij\}} A_{ij}\gamma_{ij}$ (where A_{ij} stands for the interface between regions i, j) on a triangular surface mesh assuming the volume of each cell is preserved (**see star methods, Supplemental theory and Fig 3A, D**). The resulting 3D surface meshes, which correspond to mechanically equilibrated embryos (**Fig 3D middle row**), were then intersected by a plane at half depth to generate 2D predicted cell contours that can be directly compared to confocal microcopy images (**Fig 3D bottom row**). Qualitatively, predicted shapes closely resembled observed shapes (**Fig 3D**). To quantitatively compare numerical simulations to experiments, we computed the temporal evolution of each interfacial length normalized to the total length of interfaces within the embryo. Predicted interfacial lengths matched measured lengths closely (**Fig S3C**)**,** further supporting the use of tension inference. Similar agreement between prediction and experiment was also obtained for the 2-cell stage (**Fig S3A-B)**.

To gain a better intuition into the mechanical changes that govern the evolution of the aggregate shape, we color-coded each cell interface based on its inferred tension, taking as reference the absolute tension measured for P_2 by AFM (**Fig 3D, bottom row**). This revealed that all of the surface tensions with the embryo increased with time but that the cortical tensions in ABxi and EMS increased the most. In the

compacted anterior part of the embryo, cortical tensions were larger than intercellular contact tensions; whereas, in the posterior, the cortical tension in P_2 was much lower than the tension at the EMS-P_2 interface.

In summary, the choice of a reference cell whose absolute surface tension varied little over time allowed to determine the temporal evolution of surface tensions in the whole embryo. These inferred tensions were sufficiently accurate to predict realistic embryo shapes when used as input to numerical simulations describing cell surfaces as active foams. This revealed that compaction of ABx-EMS stemmed from cortical tension increase relative to intercellular contact tension, whereas P_2 bulged out because the tension at its contact with EMS was higher than its cortical tension.

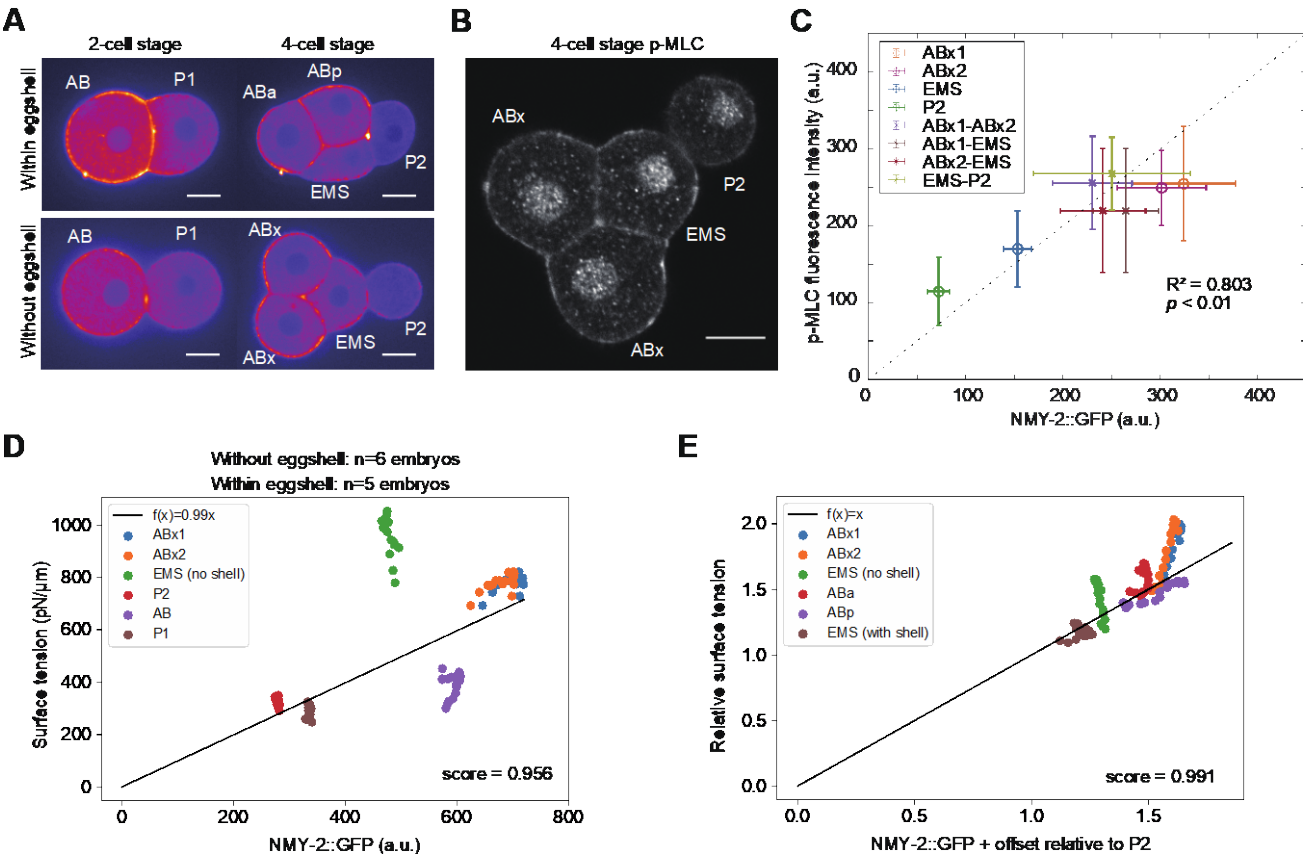

Figure 4 Surface tension correlates with myosin fluorescence intensity

A. NMY-2::GFP localization in embryos at the 2- and 4-cell stages with and without eggshell. Scale bar= 10µm. The identity of each cell is indicated on the images. Identical intensity histograms were chosen for all images. High intensities appear in yellow/red and low intensities in purple/black. **B**. Immunostaining against phosphorylated myosin light chain (p-MLC) at the 4-cell stage in an embryo outside of the eggshell. The identity of each cell is indicated on the image. Scale bar= 10µm. **C**. Phosphorylated-myosin light chain (pMLC) fluorescence intensity as a function of NMY-2::GFP fluorescence intensity in all of the surfaces of 4-cell stage embryos. Data averaged from 5 embryos. The whiskers indicate the standard deviations. The goodness of fit and its significance are indicated on the panel. **D**. Surface tension measured by AFM as a function of cortical myosin fluorescence intensity. Each data point represents one time point. Data from 3 or more embryos. The black line indicates the linear regression to the data (R^2=0.956). The coefficients of the linear regression are α=0.99 pN/µm/myo (a.u.) and β=305 pN/µm. **E**. Relative surface tension inferred from angles of contact as a function of cortical myosin fluorescence intensity. Myosin fluorescence intensity was normalized to the fluorescence intensity in the cortex of P_2. Cortical tension was normalized to the cortical tension in P_2. Data from n=6 embryos. Each data point represents one time point. The black line indicates the linear regression to the data (R^2=0.991).

Cortical enrichment in myosin correlates with cortical tension

Characterization of cell mechanics within the eggshell is not possible by AFM. Therefore, we sought to identify molecular markers that could be used to infer surface tensions within the eggshell and in later stage embryos. As the AB lineage had the highest cortical tension in our AFM measurements and

inherits most of the actomyosin (Munro et al., 2004) (**Fig S2)**, we hypothesized that cortical myosin fluorescence may be a good proxy for cortical tension. To test this, we acquired time-lapses of embryos expressing a GFP fusion to the endogenous NMY-2 gene, which encodes non-muscle myosin heavy chain, and segmented the data to obtain the temporal evolution of myosin enrichment at the cortex of each cell and at each cell-cell contact.

At 2-cell stage when the eggshell was removed, myosin fluorescence intensity in the cortex of AB was ~2-fold higher than in P_1 (**Fig 4A**, **Fig S2**), consistent with the ratio of their cortical tensions measured by AFM (**Fig 2B**). At the 4-cell stage, the ABx cells had the highest cortical myosin fluorescence, followed by EMS and finally P_2, similar to the ordering of cortical tensions measured by AFM (**Fig 2B, F**). Similar trends could also be observed for embryos within their eggshell at the 2- and 4-cell stages (**Fig S4A**). Overall, these data supported the hypothesis that cortical myosin enrichment reflects cortical tension. However, NMY-2 fluorescence is indicative of total myosin rather than the phosphorylated, active myosin, which generates tension. When we immuno-stained NMY-2::GFP embryos for phospho myosin light-chain (p-MLC, **Fig 4B**), we found that ABx cells had the highest cortical signal, followed by EMS, and P_2, similar to the ordering of cortical tensions measured by AFM. In addition, the NMY-2 and p-MLC signals showed a high degree of correlation in all of the embryonic surfaces (**Fig 4C**). Therefore, total myosin appeared as a good proxy for active myosin and differences in myosin intensity across cells appeared consistent with the differences in cortical tension measured by AFM.

Next, we quantitatively compared cortical tensions measured by AFM to myosin fluorescence intensities. For this, we plotted the cortical tensions γ_{cm} measured by AFM as a function of the fluorescence intensity i_{myo}. This revealed a positive correlation (R^2=0.956, **Fig 4D**), except for EMS that had a larger tension than expected from its NMY2 fluorescence intensity. This may occur because EMS deviates most strongly from the spherical shape that we assumed when estimating cortical tensions from AFM measurements. Importantly, these measurements allow conversion between myosin fluorescence intensities and surface tensions using the relationship $\gamma_{cm} = \alpha . i_{myo} + \beta$, where α is a linear coefficient that we assumed homogeneous within the embryo and β is a myosin-independent contribution to tension. Thus, cortical surface tensions can be inferred from myosin fluorescence images in absolute tension units. As tensions inferred from angles of contact agreed well with tensions measured by AFM (**Fig 3**), we plotted the tension inferred in each surface relative to the tension in P_2 as a function of the myosin intensity relative to P_2 (**Fig 4E**). Again, we observed a linear relationship between inferred tension and cortical myosin enrichment.

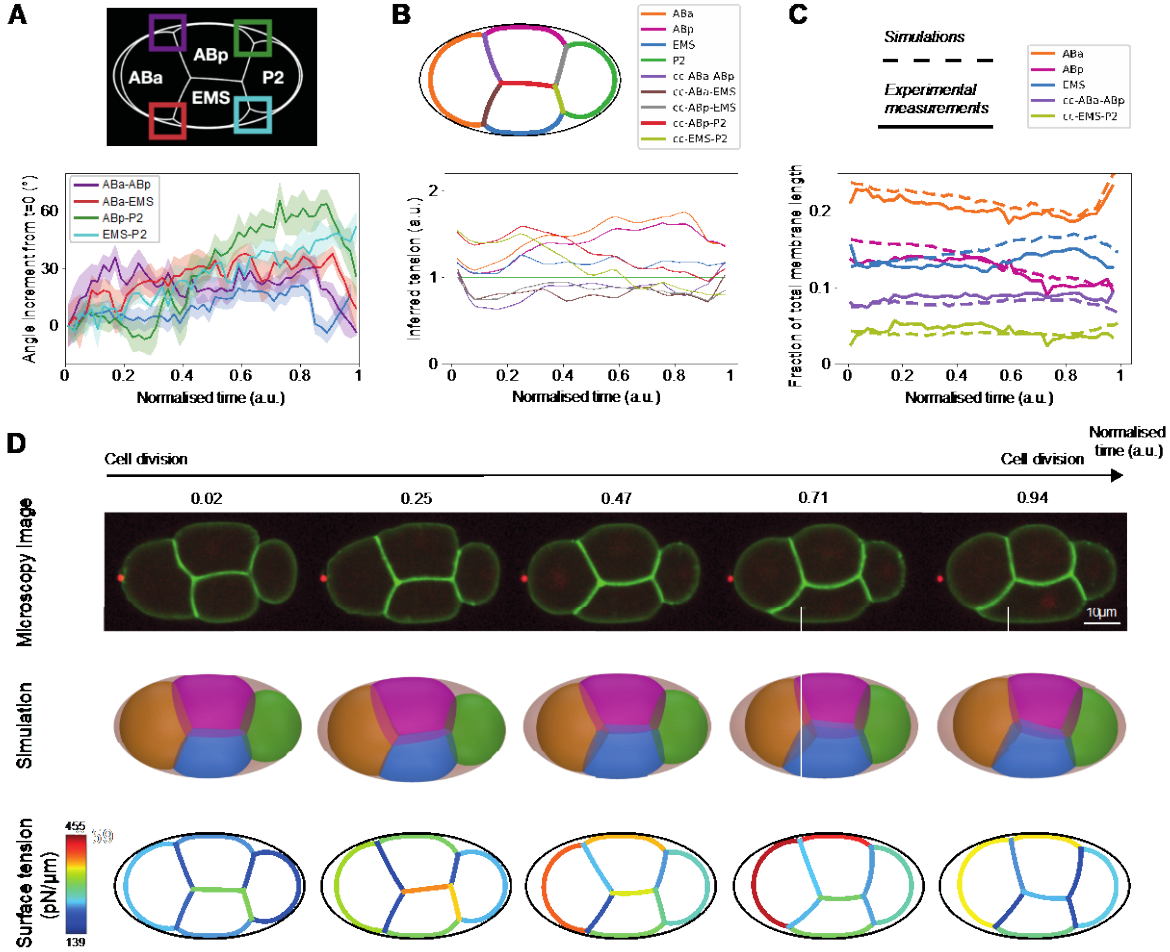

Figure 5 Prediction of morphogenesis in the eggshell

A. Temporal evolution of the change in angle of contact at trisurface junctions. Top: Schematic diagram of the 4-cell stage embryo in the eggshell. Bottom: Temporal evolution of the change in angles of contact. Time is normalized to the cell cycle. **B.** Temporal evolution of inferred surface tensions relative to P_2. Top: Schematic diagram of the 4-cell stage embryo. Each surface is color coded. Bottom: Temporal evolution of surface tensions normalized to P_2. **C.** Temporal evolution of the lengths of interfaces within the embryo at the midplane, normalized by the total interfacial length. Solid lines show experimental measurements and dashed lines show predictions from the simulations. **D.** Temporal evolution of inferred tension allows prediction of the cell arrangement in embryos within the eggshell. First row: microscopy time series of a developing embryo inside the eggshell. The membrane is visualized with GFP-PH-PLCδ (green) and the histones are visualized with mCherry::his-58 (red). Scale bar= 10 µm. Second row: temporal evolution of predicted cell arrangement within the eggshell. The eggshell appears in grey. ABa appears in yellow, ABp in pink, EMS in blue, and P_2 in green. Third row: temporal changes in absolute surface tensions obtained from myosin-informed inference. The tension in each surface is color coded with blue representing low tension and red high tension.

Myosin-informed tension inference allows prediction of morphogenesis within the eggshell

Having established that cortical tensions in *C. elegans* embryos are correlated with cortical myosin intensity (**Fig 4D**), we incorporated this information within our surface tension inference pipeline to investigate morphogenesis within the eggshell. One common challenge of tension inference approaches is to link relative tensions in time. To remedy this, we first inferred tensions within the embryo at each time point based on contact angles between the cells choosing the cortex of P_2 as a reference surface (**Fig 5A, B**). We then determined the temporal evolution of absolute cortical tension in P_2 assuming that the correlation between cortical tension and myosin intensity found outside of the eggshell remained valid (**Fig 4D**). In support of this, cortical myosin fluorescence in P_2 within the eggshell varied little over time (**Fig S4**), consistent with the small temporal changes in absolute cortical tension measured in this cell outside of the eggshell (**Fig 2F**). Combining these data allowed determination of the spatiotemporal map of all surface tensions in the embryo in absolute units (**Fig 5D,** bottom row) that closely matched the one obtained using AFM measurements (**Fig S6A-B**).

This revealed that compaction of ABa, ABp, and EMS was driven by an increase in cortical tensions coupled with a decrease in interfacial tension at cell-cell contacts, as it is outside of the eggshell (**Fig 3D**). P_2 was initially segregated from this group because the intercellular contact tensions ABp-P_2 and EMS-P_2 were larger than the cortical tension in P_2. Over time, P_2 packed more tightly with the rest of the aggregate because intercellular contact tensions decreased, likely because of the combination of an increase in cadherin at those contacts (**Fig S5A**) and a decrease in NMY-2 (**Fig S4A**). As the decrease in NMY-2 appeared concomitant with increase in E-cadherin, it may represent an indirect contribution of cadherins to the control of surface tension through regulation of myosin contractility (Sugioka and Bowerman, 2018; Yu et al., 2016).

We next predicted cell shape and arrangement in the embryo during the 4-cell stage. To mimic the presence of the eggshell, we implemented a non-penetrating ellipsoidal boundary in our simulations, that we parametrized from the average shape of the cuticle (**Supplemental theory Fig 4**). As input, we provided the temporal evolution of tensions in all surfaces (**Fig 5D bottom row**). Embryo morphologies predicted from inferred tensions closely followed experimental observations and clearly displayed the transition from a loosely linked embryo at the beginning of the 4-cell stage to a more tightly packed one at the end (**Fig 5D, middle row**). Finally, we verified that the simulations were able to accurately replicate the temporal evolution of cortical and interfacial lengths (**Fig 5C**). Overall, this indicates that the inferred tensions are sufficient to predict the morphogenesis of the early embryo and validates our foam model hypothesis. Similar results were also obtained for the 2-cell stage (**Fig S3D-**

E). Overall, these data show that myosin-informed tension inference allows an accurate prediction of morphogenesis within the eggshell without the need for direct measurements of cortical tension.

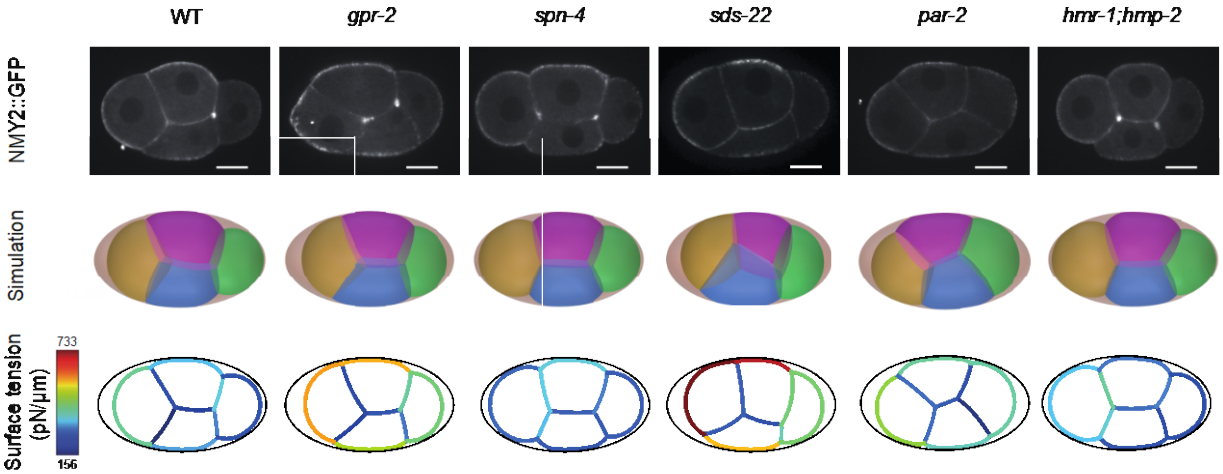

Figure 6 Myosin-informed tension inference is robust to genetic perturbations

Experimental and predicted phenotypes of embryos at the 4-cell stage for WT and gene depletions. The depleted gene is indicated above each column. Top row: Representative phenotypes of embryos expressing NMY-2::GFP at t=0.6 of the 4-cell stage. Scale bar=10µm. Middle row: Predicted phenotypes. The eggshell appears in grey. ABa appears in yellow, ABp in pink, EMS in blue, and P_2 in green. Bottom row: Absolute surface tension in each surface of the embryo. The color scale indicates the surface tension with blue colors indicating low tensions and red indicating high tensions.

Myosin-informed tension inference is robust to genetic perturbation

Next, we asked if our myosin-informed inference pipeline could predict gross changes in morphology induced by genetic perturbations. For this, we selected genes not directly affecting NMY-2 protein levels and whose depletion gave rise to a clear change in the morphology of the 4-cell embryo using a phenotypic database (Phenobank, (Sonnichsen et al., 2005)): *gpr-1/2*, *sds-22*, *par-2*, and *spn-4*, as well as *hmr-1;hmp-2* (Yamamoto and Kimura, 2017).

Depletion of three of these genes (*gpr-2*, *sds-22*, and *par-2*) gave rise to embryos more compacted than wild-type, whereas depletion of the others (*spn-4*, *hmr-1;hmp-2*) decreased compaction (**Fig 6**). We then acquired time-lapse movies of NMY-2::GFP in depleted embryos and processed them as previously to obtain the fluorescence intensity relative to WT in each cellular interface (**Fig S6C, D**). *gpr-2* and *sds-22* depletion both dramatically increased cortical myosin intensity in all cells, while leaving interfacial myosin mostly unchanged (**Fig 6A, Fig S6C**). Depletion of *par-2* led to an increase in cortical myosin in the P lineage compared to WT and a decrease in AB cells (**Fig 6A, Fig S6C**),

presumably due to inhibition of asymmetric partition of actomyosin. *par-2* depletion also decreased NMY-2 at all contacts. *spn-4* had no effect on myosin intensity at cortices or contacts, except for an increase at the ABa-ABp contact (**Fig 6A, Fig S6C**). In *hmr-1* and *hmp-2* depleted embryos, the intensity of myosin decreased at the free cortex of all cells but increased in some intercellular contacts, perhaps because of lack of E-cadherin signaling (**Fig S6C**). In summary, the depletions we examined displayed a wide variety of changes in NMY-2 in the cortex and in intercellular contacts.

We then analyzed this data using our myosin-informed inference method to determine the tension in each of the interfaces of the perturbed embryos and predicted the embryo shape (**Fig 6B**). In all cases, this predicted shape agreed well with the observed shape (**Fig 6B** middle row). The compacted phenotype of *gpr-2* and *sds-22* arose because of a generalized increase in cortical tensions relative to tensions at intercellular contacts (**Fig 6B** bottom row). In *par-2* embryos, these changes were more localized. The compacted phenotype resulted from an increase in the cortical tension in EMS and P_2 (**Fig 6B** bottom row), together with decrease in the intercellular contact tension at P_2's intercellular contacts. *spn-4* and *hmr-1;hmp-2* embryos displayed both a decrease in cortical tension and an increase in tension of some cell-cell contacts, giving rise to a decompacted phenotype.

Overall, these data indicated that phenotypes arose through a combination of changes in cortical tension and interfacial tension at cell-cell contacts. Interestingly, some phenotypes arose from changes in all of the cells of the embryo, while in others mechanics were altered in only specific cells. Compacted phenotypes emerged either from a generalized increase in cortical tension (*sds-22*, *gpr-2*) or from changes in the surface tensions of specific cells (*par-2*). Decompacted phenotypes (*spn-4, hmr-1;hmp-2)* resulted from a global decrease in cortical tension combined with an increase in intercellular tensions.

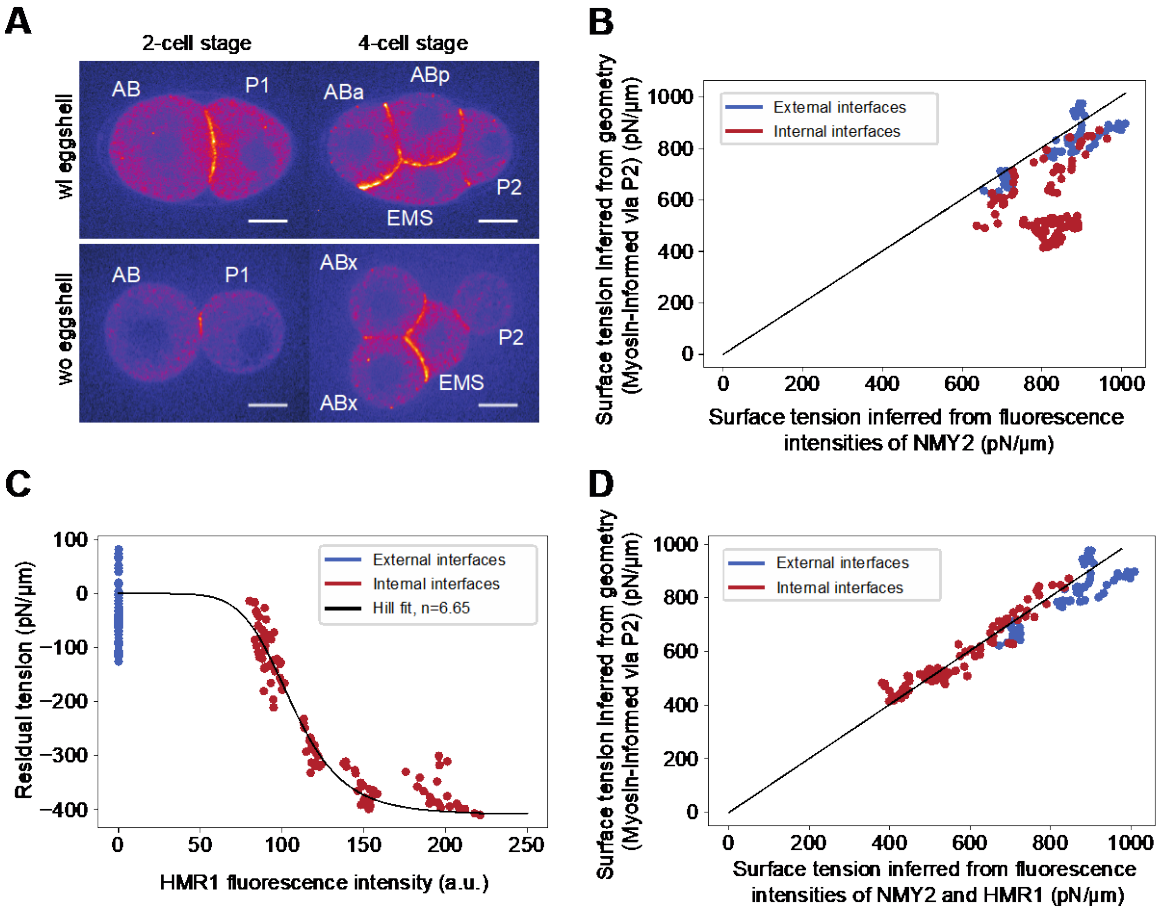

Figure 7: E-cadherin contributes non-linearly to surface tension at intercellular contacts. A. E-cadherin-GFP (HMR-1) localization in embryos at the 2 and 4 cell stages with and without eggshell. Scale bar= 10µm. The identity of each cell is indicated on the images. Identical intensity histograms were chosen for all images. High intensities appear in yellow/red and low intensities in purple/black. **B**. Surface tension inferred from geometry as a function of surface tension inferred from myosin fluorescence intensity. Blue dots indicate cortical tensions and red dots tension at cell-cell contacts. The solid black line shows the line of slope 1. **C**. Residual tension in embryo surfaces as a function of E-cadherin fluorescence intensity. Fluorescence intensity of the background was removed from the signal in the embryo. Blue dots indicate cortical tensions and red dots tension at cell-cell contacts. **D**. Surface tension in embryonic surfaces as a function of myosin and E-cadherin fluorescence intensity. Blue dots indicate cortical tensions and red dots tension at cell-cell contacts. The solid black line shows the line of slope 1.

Cell-cell contact tension depends non-linearly on E-cadherin enrichment

We next investigated if the interfacial tensions we computed (**Fig 5**) could be determined from molecular information. In *C. elegans* early embryos, cells are linked to one another via E-cadherin adhesion complexes. Cadherins can decrease surface tension directly by increasing adhesion between cells and indirectly by decreasing myosin activity via downregulation of RhoA downstream of recruitment of p120-catenin by the cadherin cytoplasmic domain (Yu et al., 2016). Previous work in Drosophila suggested that cadherins contributed both directly and indirectly to tension at cell-cell

contacts (Chan et al., 2017); whereas, in other organisms (such as mouse and zebrafish), cadherin-mediated adhesion only contributes indirectly through its regulation of myosin contractility at cell-cell contacts (Maitre et al., 2012).

First, we examined the temporal evolution of HMR-1 (E-cadherin) enrichment at intercellular contacts by acquiring time-lapses of embryos with a GFP fusion to the endogenous *hmr-1* gene, and processing the data in the same way as for NMY-2 (**Fig 7A**). We then asked if there was a direct correlation between the evolution of tension at intercellular contacts and HMR-1 enrichment. At the onset of the 2-cell stage outside of the eggshell, the HMR-1 signal at the AB-P_1 contact was initially indistinguishable from cytoplasmic background before gradually increasing until reaching a plateau mid-way through interphase when the contact became visible (**Fig S5B**). This temporal evolution contrasted with the gradual increase in the interfacial tension γ_{cc} inferred at this contact after t~0.5 (**Fig S3C**). At the 4-cell stage outside of the eggshell, HMR-1 fluorescence was highest at the contacts between the ABx cells and EMS, followed by the contact between the ABx cells, and weakest in EMS-P_2 (**Fig S5B**). During interphase, HMR-1 enrichment in the contacts between ABx and EMS decreased by about 50% (**Fig S5B**), in contrast to the stable intercellular tension measured at these contacts. At the ABx-ABx contact, the HMR-1 signal stayed constant, as did the contact tension between these two cells. In contrast, at the EMS-P_2 contact, the HMR-1 signal was initially indistinguishable from cytoplasmic background before steadily increasing throughout interphase, similar to tension. Interestingly, the contact between EMS and each of the ABx cells was not exactly similar, perhaps indicating that despite the absence of an eggshell some differences subsist between the two daughters of AB. Similar trends were also observed for cell-cell contacts within the eggshell at the 2- and 4-cell stages, except that the HMR-1 signal remained constant at the EMS-ABa and EMS-ABp contacts. Overall, the temporal evolution of HMR-1enrichment did not appear to follow a consistent pattern of correlation with tension at cell-cell contacts, suggesting that HMR-1 is not the only factor regulating cell-cell interfacial tension. We hypothesized that this may be because HMR-1 was interfaced to the F-actin cytoskeleton in some contacts but not in others. Therefore, we imaged the spatiotemporal localization of HMP-1 and HMP-2 (α- and β- catenin) that link E-cadherin to F-actin. However, their enrichment at contacts mirrored in all points that of HMR-1 (**Fig S5C-E**). Overall this suggested a complex relationship between interfacial tension and cadherin localization.

Next, we investigated if tension at intercellular contacts could be predicted solely based on myosin enrichment, reasoning that any regulation emanating from E-cadherin should be reflected in the levels of myosin. We hypothesized that myosin's contribution to interfacial tension was identical to its contribution to cortical tension (**Fig 4C**). We then plotted the interfacial tension at cell-cell contacts as

a function of the myosin intensity at contacts (**Fig 7B**). This revealed that actual interfacial tensions were systematically lower than predicted from myosin enrichment, suggesting a potential direct negative contribution of cadherin. To estimate a potential direct contribution, for each cell-cell contact, we computed a residual tension not due to myosin by calculating: $\gamma_{residual} = \gamma_{cc} - (\alpha . i_{myo_contact} + \beta)$. We then plotted $\gamma_{residual}$ as a function of the intensity of cadherin (**Fig 7C**). This revealed that the residual tension decreased with increasing cadherin intensity until reaching a plateau at the highest levels of cadherin enrichments. This relationship could be well fit with a Hill function of the form $\frac{L}{1+(K/(i_{HMR-1}-w))^n}$ with L=-410 pN/µm the maximal decrease of surface tension at infinite concentration, K the HMR-1 intensity at which half of the maximal decrease in obtained, i_{HMR-1} the intensity of HMR-1, w the background level of HMR-1, and n=6.65 the Hill coefficient. Interestingly, this large Hill coefficient suggests a possible cooperativity effect in the direct contribution of cadherin to cell-cell interfacial tensions. Incorporating the contribution of cadherins and myosins using both empirical relationships allowed accurate prediction of all surface tensions in the embryo based on myosin and cadherin intensities (**Fig 7C**).

In summary, interfacial tension was set by myosin, whose enrichment was affected by cadherin-mediated signaling, together with a direct negative contribution of cadherins.

Discussion

C. elegans is an organism that develops rapidly within an eggshell and in which cells undergo a fixed lineage specification resulting in embryos with a characteristic cellular arrangement. By performing direct mechanical measurements alongside quantitative imaging, we validate the use of tension inference for predicting the relative tension in cells and show that cortical tension correlates with the abundance of myosin at the cortex. Incorporating information about the evolution of cortical tension determined from myosin intensity within our inference framework allows to reconstruct the temporal evolution of absolute tension in all of the surfaces of the embryo both in and out of the eggshell. In turn, knowledge of these surface tensions is sufficient for accurate prediction of the temporal evolution of the cell shape and cellular arrangement in the embryo. Importantly, this myosin-informed tension inference framework allows to predict the impact of genetic manipulations on cell arrangement and shape within the embryo. We then exploited our approach to reveal a direct contribution of cadherins to interfacial tension at cell-cell contacts, in the form of a non-linear decrease in tension with increasing cadherin enrichment.

Spatiotemporal mechanical changes in the early *C. elegans* embryo

Myosin-informed surface tension inference allowed us to draw a panorama of the spatiotemporal mechanics of the early *C. elegans* embryo. Importantly, this knowledge allowed accurate prediction of the evolution of cell shape and cell arrangement over time. At the 2-cell stage, tension in the AB cell was several fold larger than in the P_1 cell, likely because of the asymmetric partition of actomyosin that takes place during the first division. At the 4-cell stage, a second asymmetric division gives rise to P_2 and EMS, whose mechanics differ dramatically and potentially point to differences in regulation of myosin contractility downstream of fate specification. The surface tension in both of these cells was initially lower than in ABa and ABp, the progeny of the AB cell. However, the cortical tension in EMS increased dramatically over time, while the cortical tension in P_2 remained low. The changes in EMS occurred simultaneously with an increase the surface tension in ABa and ABp and a decrease in the tension of the ABa-ABp, ABa-EMS, and ABp-EMS contacts. Thus, compaction of ABa, ABp, and EMS was driven by the combination of an increase in cortical tension in these cells together with a decrease in the tension at their contacts. Conversely, P_2 remained separate from this aggregate because its absolute cortical tension remained lower than the tension at its contacts with EMS and ABp. This was particularly apparent in embryos without an eggshell, in which the cortical tension in P_2 was 1.5 fold lower than in the EMS-P_2 contact. The low cortical tension in P_2 is intriguing as it is a type of stem cell and maintenance of pluripotency in mammalian *in vitro* stem cell culture relies on inhibition of contractility and a low surface tension (Maitre et al., 2016; Zhu and Zernicka-Goetz, 2020). Therefore, as in mammalian systems, differentiation of cells in *C. elegans* appears to involve an increase in surface tension.

Rules of morphogenesis

Our careful characterization of the mechanics of embryos characterized the mechanical origin of changes in cell arrangement. Decompaction was observed in *spn-4* depletion and *hmr-1;hmp-2* depletions driven by a global decrease in cortical tension coupled to an increase in tension at cell-cell contacts. Intriguingly, the same phenotypes could arise from distinct mechanical changes. For example, we observed compacted phenotypes when we depleted *par-2*, *sds-22*, and *gpr-2*, genes that target very different processes When we determined the surface tensions in the 4-cell stage embryos exposed to these perturbations, we found compaction in response to *sds-22* and *gpr-2* depletion arose from a generalized increase in cortical tension. In contrast, compaction in *par-2* depleted embryos was driven by an increase in the cortical tension of posterior cells and a decrease in their contact tension. Therefore, a careful examination of the exact mechanical changes is necessary to understand phenotypic change and it will be interesting to determine whether each distinct mechanical signature occurs through specific changes in signaling.

Direct and indirect contributions of cadherins to tension at intercellular contacts

Cadherin-mediated adhesion can in principle contribute both directly and indirectly to surface tension at intercellular contacts. While in some model systems, cadherins mostly contribute to intercellular contact tension indirectly by regulating myosin activity; in others, they contribute directly. Examining cellular mechanical changes alongside molecular reporters of contractility and adhesion enabled us to quantify the direct and indirect contributions of cadherins to tension at intercellular contacts.

The indirect contribution of cadherins at contacts could be evidenced by plotting the interfacial tension as a function of the tension expected from its myosin enrichment using the relationship found for cortical tension. This systematically overestimated the tension, signifying that another molecular process decreased interfacial tension. Therefore, we computed the residual tension defined as the actual tension minus the tension expected from myosin enrichment. As expected from theoretical considerations, the direct contribution of cadherins reduced tension at cell-cell interfaces. Intriguingly, when we plotted the direct cadherin contribution to interfacial tension as a function of cadherin enrichment, we found that it decreased rapidly at a certain threshold before saturating for higher intensities. This behavior, reminiscent of a Hill-Langmuir function, suggests a Michaelis-Menten binding kinetics with strong cooperativity (Hill coefficient $n>6$), that could be due to the cooperative cis-binding of cadherins (Thompson et al., 2021). Interestingly, saturation for high cadherin enrichment is consistent with the observation that HMR-1 overexpression does not cause any phenotypic change (Padmanabhan et al., 2017). Although, beyond a certain density, further enrichment of cadherins no longer directly changes surface tension, it will be interesting to determine if saturation is also observed in the indirect contributions that arise through regulation of myosin activity.

Conclusion

Overall, our study characterizes the dynamic mechanical changes that take place in the early *C. elegans* embryo and evidences the direct contribution of cadherins to interfacial tension. Our modeling approaches pave the way for a quantitative understanding of mechanical robustness during development.

Author contributions

KY, HT, and GC conceived and designed the study. KY did most of the experiments and initial data analysis. SI and HT designed and carried out the force inference and numerical simulations and wrote the Supplemental information. KY, SI and FD performed the data analysis. JP and NG carried out control experiments. KY, HT, and GC wrote the manuscript. All authors commented on the manuscript.

Acknowledgements

We thank past and present members of the Charras and Turlier labs for comments and discussions. We thank Dr Grégoire Michaux (IGDR, Rennes, France) for discussions during the study and feedback on the manuscript. We also thank Prof. Akatsuki Kimura in National Institute of Genetics for kind supports to KY. KY was supported by a Grant-in-Aid for JSPS Fellows (16J09469) and research grants from the Uehara Memorial Foundation. KY was supported by a European Research Council consolidator grant (CoG-647186) to GC. NWG is supported by the Francis Crick Institute that is supported by the Francis Crick Institute (N.W.G.), which receives its core funding from Cancer Research UK (FC001086), the UK Medical Research Council (FC001086), and the Wellcome Trust (FC001086). SI was supported by a PSL-UCL doctoral internship programme. HT and FB are supported by the CNRS and Collège de France. HT has received funding from the European Research Council (ERC) under the European Union's Horizon 2020 research and innovation programme (Grant agreement No. 949267). Some *C. elegans* strains were provided by the CGC, which is funded by NIH Office of Research Infrastructure Programs (P40 OD010440). FL238 was kindly provided by Drs Anne Pacquelet and Grégoire Michaux Group in IGDR, Université de Rennes, France.

Declaration of interests

The authors declare no competing interests.

Supplemental figures

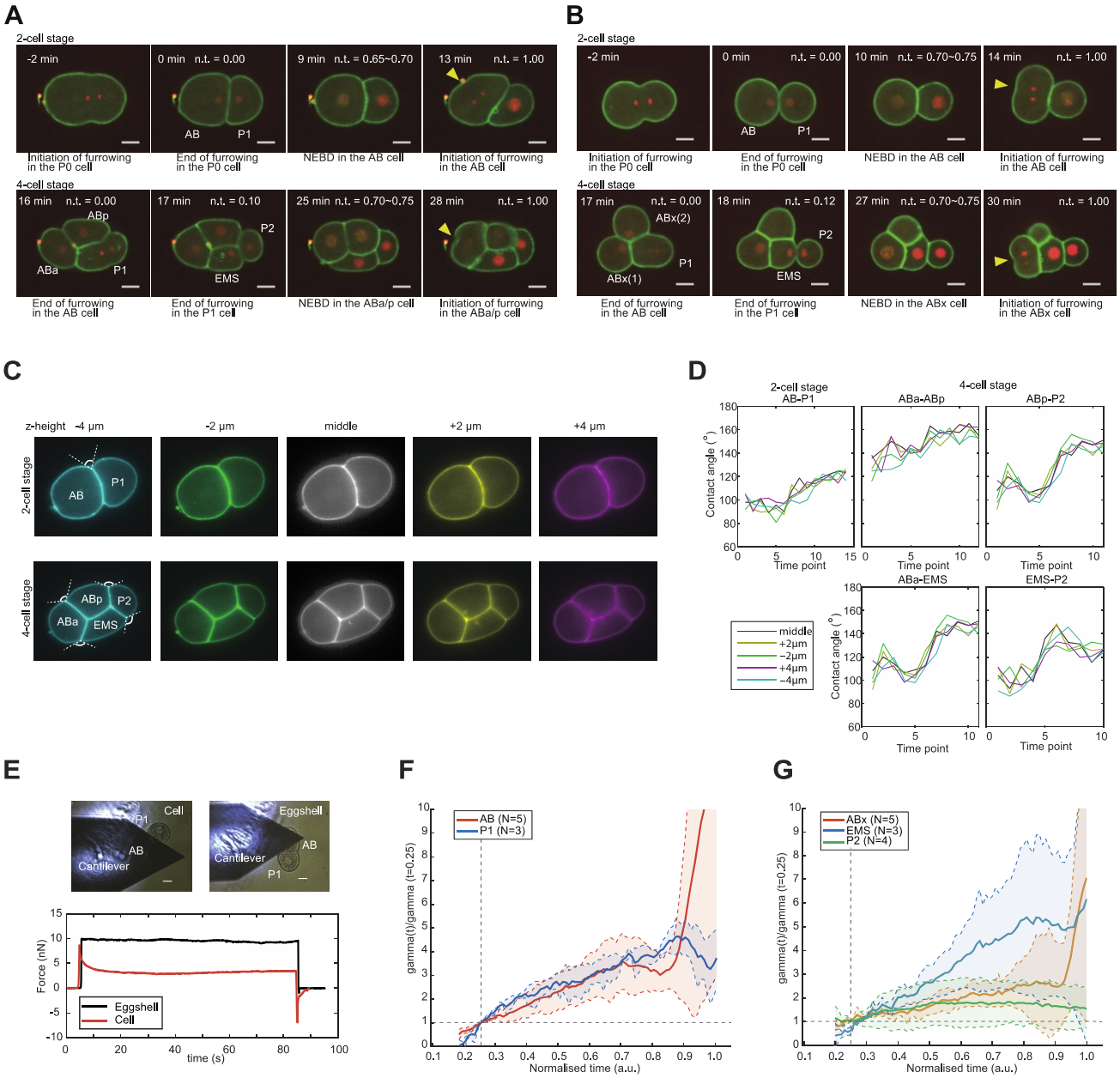

Figure S1 related to Figures 1 and 2. **(A-B)** Representative evolution of the cell arrangement in 2- and 4-cell *C. elegans* embryos. Cell membranes are visualized using GFP-PH-PLCδ and nucleic acids are visualized using mCherry::his-58. Scale bars =10µm. Yellow arrowheads indicate the position of furrowing. Cell names are indicated on each panel. Actual times are indicated in the top right corner. Normalized times (n.t.) are indicated in the top right corner. For the 2-cell stage, n.t.=0 was chosen as the time when P_0 finishes its division and for the 4 cell-stage, it was chosen as the time when AB finishes its division. For the 2-cell stage, n.t.=1 was chosen as the time when AB starts to furrow and, for the 4-cell stage, it was chosen as the moment when ABa/p begins to furrow. **A**. Representative evolution of cell arrangement for *C. elegans* embryos in the eggshell. **B**. Representative evolution of cell arrangements for *C. elegans* embryo outside of the eggshell. **C**. Consecutive images of a confocal microscopy stack taken at different optical planes. The position of each plane is given relative to the mid-plane of the embryo. Top row: 2-cell stage. Bottom row: 4-cell stage. The name of each cell is indicated

on the left most image. The angles of contact are displayed in the leftmost column. **D**. Temporal evolution of the angles of contact shown in C. Each line represents a different optical plane. Angular evolution is not affected by small differences in the optical plane chosen for measurement. **E**. Representative AFM measurement of the mechanics of a cell and the eggshell. Top row: representative brightfield images of an AFM cantilever in contact with a 2-cell stage embryo without (left) and with (right) an eggshell. The name of each cell is indicated on the images. Scale bar=10µm. Bottom row: Representative graph showing the temporal evolution of the deflection force sensed by the AFM cantilever for a cell in an embryo without an eggshell (orange) or for the eggshell (blue). The cantilever is initially out of contact and senses no force. It is then brought into contact with the cell or the eggshell at t~5s, leading to an increase in the measured force. The cantilever is then kept at a constant height for 80s before being retracted, leading to a return of the force to 0. While the cantilever is in contact, the force measured on the cell decreases due to viscoelastic relaxation stemming from biological processes such as cytoskeletal turnover. In contrast, no such relaxation is observed on the eggshell pointing to a solid-like behavior. **F**. Temporal evolution in surface tension in cells of a 2-cell stage embryo relative to the surface tension at n.t.=0.25. Solid lines indicate the average and shaded areas the standard deviation. Data from Fig 2D. **G**. Temporal evolution in surface tension in cells of a 4-cell stage embryo relative to the surface tension at n.t.=0.25. Solid lines indicate the average and shaded areas the standard deviation. Data from Fig 2E.

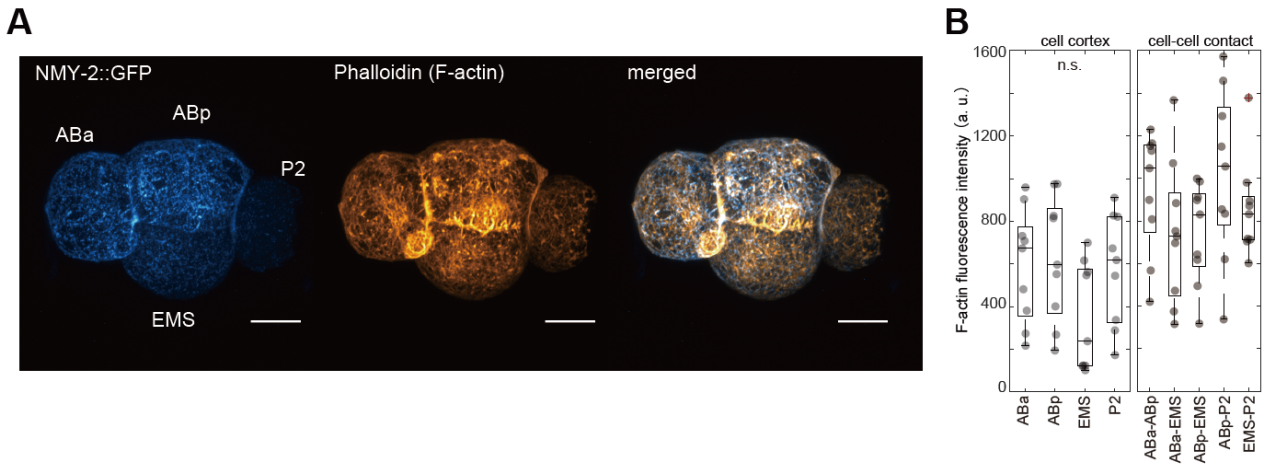

Figure S2 related to Figure 2: **Actomyosin distribution in 4-cell stage C elegans embryos.** The name of each cell is indicated on the images. Scale bar = 10µm. **A.** Left: Myosin distribution in the embryo. Myosin was visualized by imaging GFP fluorescence Middle: F-actin distribution in the embryo. F-actin was visualized by staining with phalloidin. Right: Overlay of the two stains. **B.** F-actin fluorescence intensities measured in the cortex of each cell (left) and at each cell-cell contact (right). Data from 9 embryos. There were no significant differences in F-actin fluorescence intensity in cell cortices or at cell-cell contacts. Multiple t-tests with Bonferroni correction.

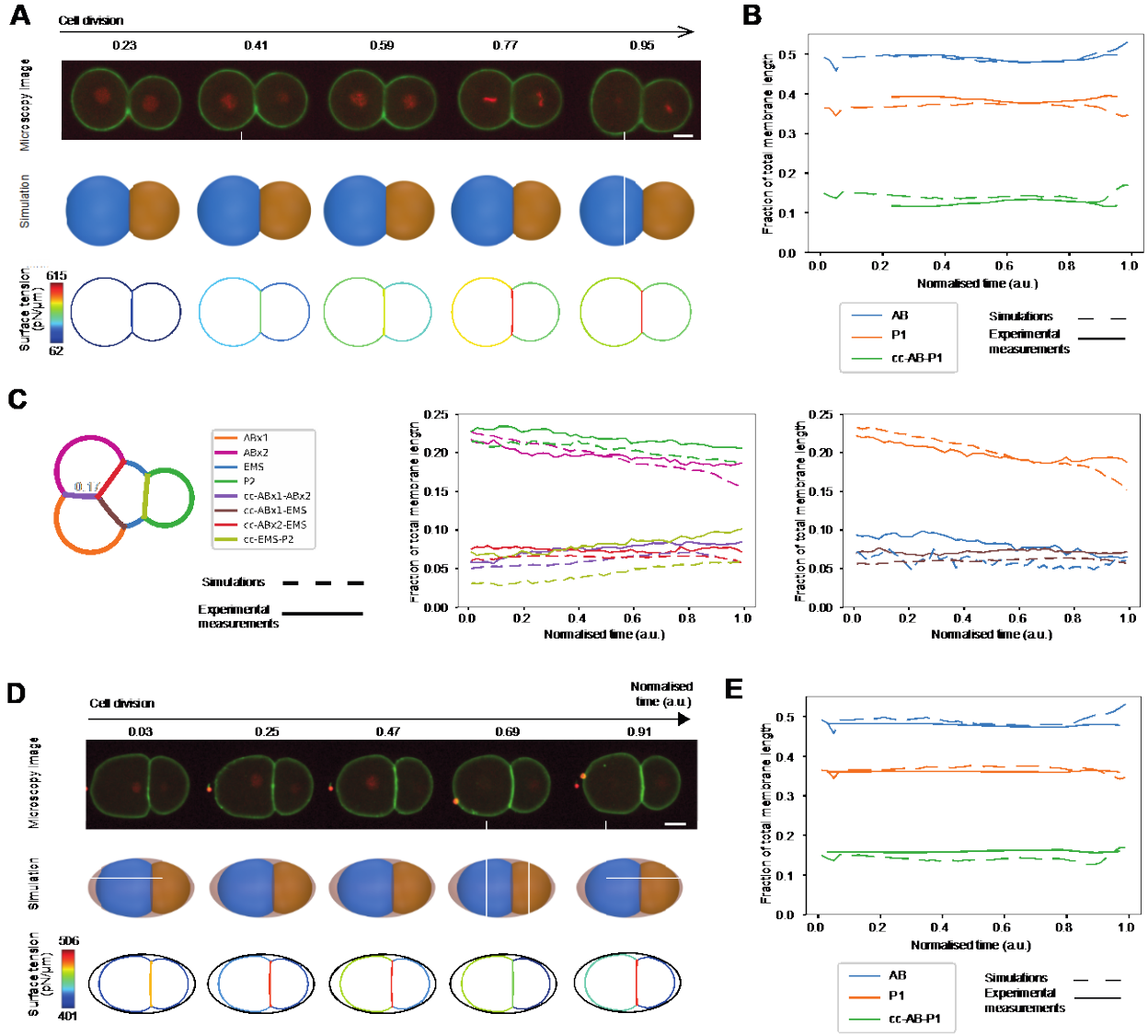

Figure S3 related to Figures 3 and 5: **A**. Temporal evolution of inferred tension allows prediction of the cell arrangement in embryos outside of the eggshell. First row: microscopy time series of a developing embryo outside of the eggshell. The membrane is visualized with GFP-PH-PLCδ (green) and the histones are visualized with mCherry::his-58 (red). Scale bar=10µm. Second row: temporal evolution of predicted embryo shape. AB appears in blue, and P_2 in orange. Third row: temporal changes in surface tension in pN/µm. The tension in each surface is color coded with dark blue representing low tension and red high tension. **B.** Temporal evolution of the interface length for the free surface of AB (blue), the free surface of P1 (orange), and the intercellular contact (green). Experimental measurements appear as solid lines and simulations as dashed lines. Data from 6 embryos. **C.** Fraction of the total interfacial length contributed by each cellular interface in experiments and simulations for 4-cell stage embryos without eggshell. Experimental measurements are shown as solid lines and simulations as dashed lines. Middle and right: temporal evolution of the interfacial lengths. Color codes are indicated on the left. Data from 6 embryos. **D.** Temporal evolution of inferred tension allows prediction of the cell

arrangement in embryos within the eggshell. First row: microscopy time series of a developing embryo inside the eggshell. The membrane is visualized with GFP-PH-PLCδ (green) and the histones are visualized with mCherry::his-58 (red). Scale bar=10μm. Second row: temporal evolution of predicted embryo shape. The eggshell appears in grey. AB appears in blue and P_1 in brown. Third row: temporal changes in surface tension in pN/μm. The tension in each surface is color coded with blue representing low tension and red high tension. **E**. Temporal evolution of the normalized lengths occupied by each surface within the embryo. Solid lines show experimental measurements and dashed lines show predictions from the simulations. Data from 5 embryos.

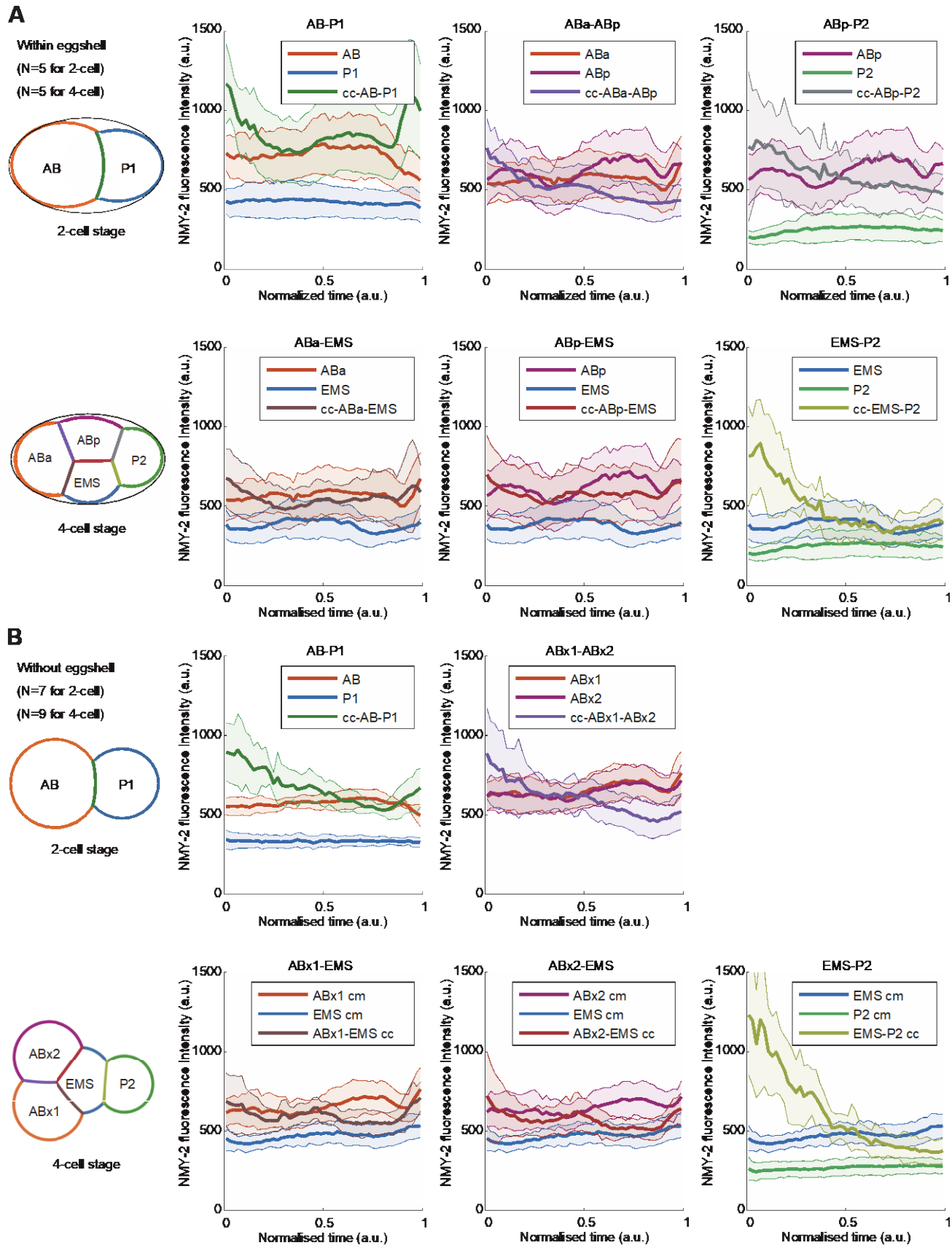

Figure S4 related to Figure 4: Temporal evolution of NMY-2 in the surfaces of the 2- and 4-cell *C. elegans* embryos with and without eggshell. The pictograms in the left column indicate the color code for the surfaces of the embryo. In all graphs, the solid line is the average and the shaded region depicts the standard deviation. N≥5 embryos for each

condition. Each graph shows the evolution of the fluorescence intensity of myosin in an intercellular contact (indicated as cc) and in the cortices on either side of that contact (indicated as cm). All intensities are given in a.u. **A.** Temporal evolution of NMY-2 fluorescence intensity in 2- and 4-cell stage embryos within the eggshell. **B.** Temporal evolution of NMY-2 fluorescence intensity in 2- and 4-cell stage embryos outside of the eggshell.

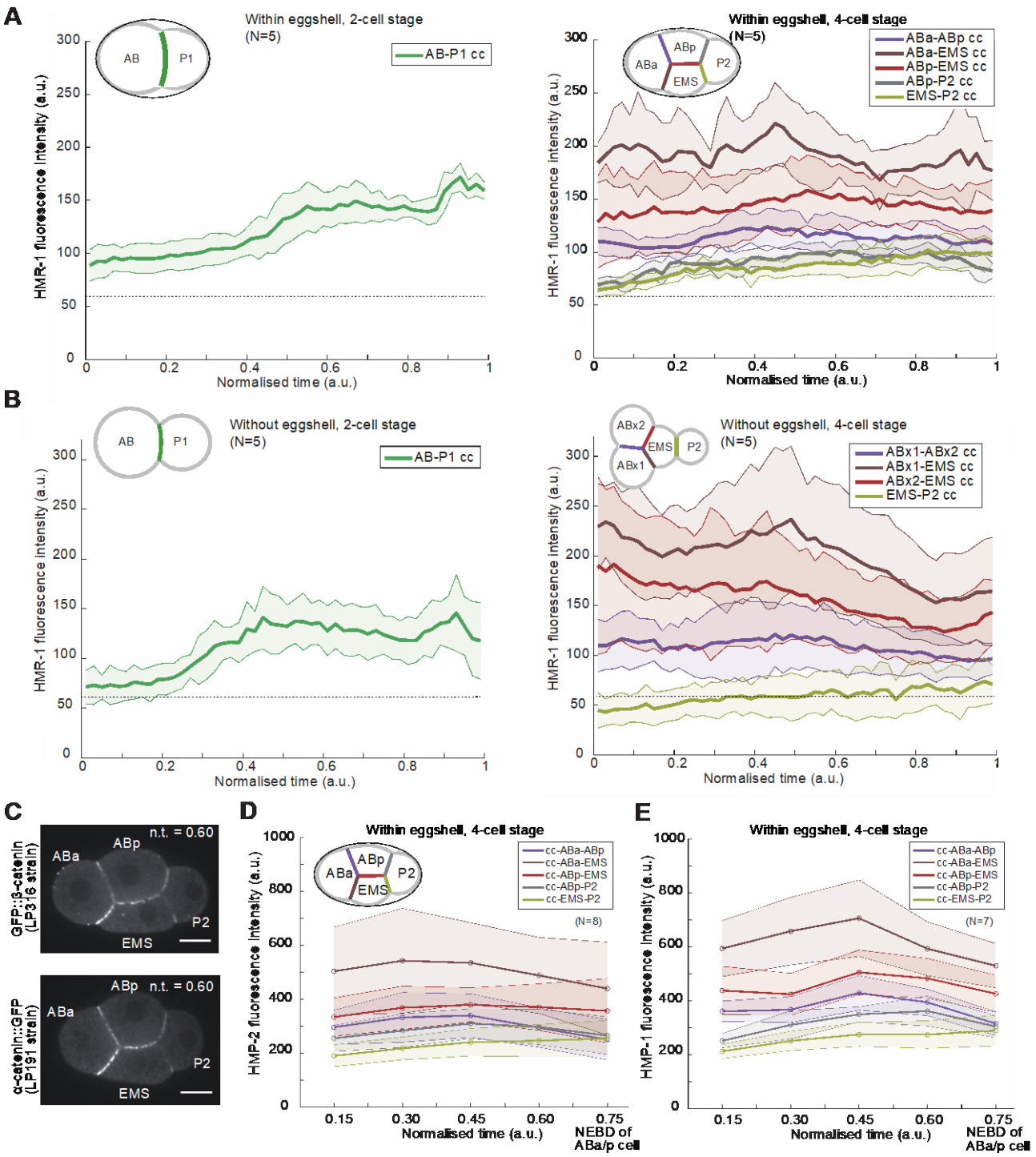

Figure S5 related to figure 7: **Temporal evolution of HMR-1, α-catenin, and β-catenin at cell-cell contacts in the *C. elegans* embryos. (A-B)** In all panels, the inset pictogram indicates the position of cell-cell contacts in the embryo. The solid line is the average and the shaded region depicts the standard deviation. N=5 embryos for each condition. The black dashed line indicates the cytoplasmic fluorescence of HMR-1. **A.** Left: temporal evolution of HMR-1 fluorescence intensity at the AB-P_1 contact for an embryo with an eggshell. Right: Temporal evolution of HMR-1 fluorescence intensity at the cell-cell contacts in the 4-cell stage embryo with an eggshell. **B.** Left: Temporal evolution of HMR-1 fluorescence intensity at the AB-P_1 contact for an embryo without an eggshell. Right: Temporal evolution HMR-1 fluorescence intensity at the cell-cell contacts in the 4-cell stage embryo without an eggshell. **C**. Top: Representative images of β-catenin (HMP-2) in

the 4-cell *C. elegans* embryo with an eggshell. Bottom: Representative images of α-catenin (HMP-1) in the 4-cell *C. elegans* embryo with an eggshell. Scale bars=10μm. **D**. Temporal evolution HMP-2 fluorescence intensity at the cell-cell contacts in the 4-cell stage embryo with an eggshell. The solid line is the average and the shaded region depicts the standard deviation. Data from N=8 embryos. **E**. Temporal evolution HMP-1 fluorescence intensity at the cell-cell contacts in the 4-cell stage embryo with an eggshell. The solid line is the average and the shaded region depicts the standard deviation. Data from N=7 embryos.

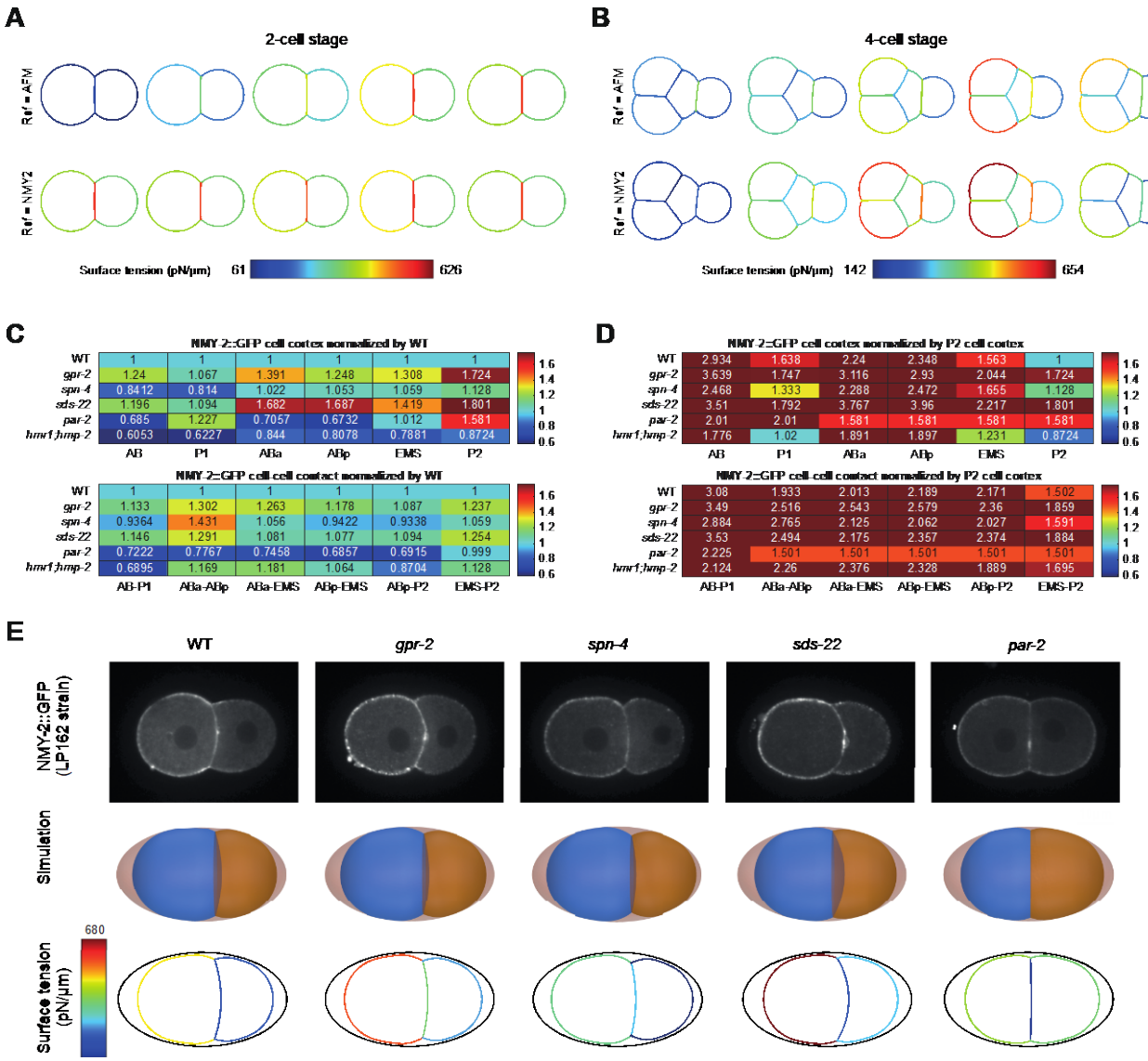

Figure S6 related to Figures 5-7: **(A-B)** Temporal evolution of tensions at interfaces of the 2- and 4-cell embryos without an eggshell using the tension measured by AFM or inferred from myosin intensity as reference. All surfaces are colored according to their tension. **A.** Top row: Temporal evolution of surface tension in the 2-cell embryo computed choosing the cortical tension measured by AFM in P_1 at t=0 as reference. Bottom row: Temporal evolution of surface tension in the 2-cell embryo computed choosing the tension inferred from myosin fluorescence at the cortex of P_1 at t=0 as reference. **B.** Top row: Temporal evolution of surface tension in the 4-cell embryo computed choosing the cortical tension measured by AFM in P_2 at t=0 as reference. Bottom row: Temporal evolution of surface tension in the 4-cell embryo computed choosing the tension inferred from myosin fluorescence at the cortex of P_2 at t=0 as reference. **(C-D).** Impact of gene depletion on myosin fluorescence intensity at embryo surfaces. In all tables, the depleted gene is indicated on the left of each row and the cell surface is indicated at the bottom of each column. Grid positions are color coded based on the extent of change. **C.** Myosin fluorescence intensity in each cell surface relative to the same surface in the WT embryo. **D.** Myosin fluorescence intensity in each cell surface relative to the free surface of P_2 in WT. **E.** Experimental and predicted phenotypes of embryos at the 2-cell stage for WT and gene depletions. The depleted gene is indicated above each column. Top row: Representative

phenotypes of embryos expressing NMY-2::GFP at t=0.6 of the 2-cell stage. Scale bar= 10 μm. Middle row: Predicted phenotypes. The eggshell appears in grey. AB appears in blue and P_1 is brown. Bottom row: Surface tension in each surface of the embryo. The color scale indicates the surface tension with high tensions in red and low tensions in blue. Cortical tension in P_1 in each of the depleted embryos was inferred based on its NMY-2 fluorescence intensity.

Materials & Methods

C. elegans strains

The *C. elegans* strains used for this study are listed in Table S1. *C elegans* were maintained using a standard procedure for *C. elegans* culture (Brenner, 1974; Stiernagle, 2006). Briefly, worms were kept on NGM agar plates seeded with OP50 E. coli at 20C until use. *C. elegans* embryos were dissected from adult worms and collected in 0.75× egg salt (118 mM NaCl, 40 mM KCl, 3.4 mM CaCl2, 3.4 mM MgCl2, 5 mM HEPES pH 7.2) under the stereoscopic microscope.

RNA interference

RNA interference for *par-2*, *hmr-1*, *hmp-2*, *gpr-2*, *sds-22*, *spn-4* was done by the standard feeding method (Kamath et al., 2001). The C. elegans RNAi library (Source BioScience, Nottingham, UK) was used (Fraser et al., 2000). For *hmr-1* RNAi, the E. coli strain described previously was used (Yamamoto and Kimura, 2017). Briefly, E-coli were seeded on NGM-IPTG plate and they were kept at room temperature overnight before use. *C. elegans* larvae at L3~L4 stage were plated on the plates and kept at 20C for 30 to 36 hours before dissection.

Eggshell removal

Eggshell was removed using a previously described method with modification (Park and Priess, 2003). Briefly, gravid worms were dissected in 0.75x Egg salt and 1-cell or 2-cell stage embryos were collected using mouth-pipette. The embryos were treated in bleach mix for 90 seconds. Then the embryos were washed in Shelton's growth medium (SGM) (Shelton and Bowerman, 1996) three times. Lastly, a fine glass capillary (GD-1; Narishige, Tokyo, Japan) was pulled on a Sutter Flaming brown pipette puller. The embryos were imaging on a stereoscopic microscope and the glass capillary was used to remove the eggshell with mouth pipetting. The cells were then kept in SGM before use at room temperature.

Atomic Force Microscopy

For cell-medium cortical tension measurements, firstly the eggshell was removed at the 1-cell stage or 2-cell stage. Next, the embryos were transferred to a glass bottom Petri dish (WPI, Sarasota, FL, USA) filled with 0.75x Egg salt with a drop of SGM. Tension measurements were performed with a CellHesion atomic force microscope (JPK instruments, Berlin, Germany) mounted on an IX81 inverted microscope (Olympus, Japan) equipped with a FV1000 confocal laser scanner unit. Flat cantilevers with a nominal spring constant of k=0.03 N/m (Arrow TL1Au, Nanoworld, Neuchâtel, Switzerland) were used for measurements. The sensitivity was calibrated by acquiring a force curve

on a glass coverslip and the spring constant was calibrated using the thermal noise calibration method implemented in the AFM controller software. Two types of cortical tension measurements were performed: short-term compression experiments were used to measure cortical tension at a given time point and long-term compression experiments to follow the temporal evolution of cortical tension.

In short-term compression measurements, a force curve was acquired on the glass surface next to the cell of interest to allow for determination of cell height. Next, the cantilever was positioned above the cell of interest, the cantilever was approached towards to cell at a speed of 5 μm/s with a force setpoint of 10 nN. On average, cell height was reduced by 20 to 30% by application of force. After contact, force relaxed rapidly before reaching a plateau after ~30s, consistent with previous reports on mammalian cells (Fischer-Friedrich et al., 2014). The mean value of the force between 30-70 s after contact was used as input to calculate cell-medium cortical tension. After 80s contact, the cantilever was retracted. The maximum cell radius during compression was obtained from a bright field image. The height of the cell before and during compression was measured following the method in (Stewart et al., 2011).

Long-term compression experiments used the same experimental protocol, except that the cantilever remained in contact with the cell until division. In these experiments, EG4601 embryos expressing GFP::H2B were imaged with the confocal microscope (a FV1000 laser scanning confocal head mounted on an IX81 microscope) to monitor the evolution of the cell cycle during compression. A force setpoint of 5 nN was chosen. To keep the temperature of the medium below 25C, a custom-made temperature cooler was employed. The maximum cell radius and cell height were measured as described above to calculate cell-medium cortical tension.

Cortical tension calculation

The full derivation of the formula to calculate the cortical tension is detailed in the SI. Here, we do not make any geometric approximation for the shape of the profile (Fischer-Friedrich et al., 2014), but we solve for the true Laplace's profile, following (Norotte et al., 2008). The cell is characterized by a cortical tension γ and is compressed by an AFM cantilever with a height h with a force F. We suppose that the adhesion of the cell to the substrate and to the AFM cantilever are negligible, such that the contact angle $\theta = 0$. The maximum cell radius at the midplane parallel to the AFM cantilever is measured optically (see above) and denoted by r_1. The free radius of the cell, measured before compression is denoted by r_0.

The tension is given by force balance at the midplane and reads:

$$\gamma = \frac{F}{2\pi r_1(\alpha - 1)}$$

where α is a dimensionless parameter, which is determined using the AFM height h and the planar radius in the midplane r_1 (see **Supplemental theory**).

Live cell imaging

A spinning disk confocal microscope was used to acquire time-lapse images for LP162, LP172 and FL238 strains. For embryos with an eggshell, 1-cell stage embryos were placed in 0.75x egg salt on a 1% agar gel pad and this was gently covered with a coverslip. For embryos whose eggshell had been removed, embryos were placed in SGM on the coverslip, this was then covered by another coverslip and sealed with valap (1:1:1 mixture of petroleum jelly:lanolin:paraffin wax) to prevent drying. Embryos were imaged at room temperature with a spinning-disk head (CSU-10, Yokogawa, Japan) mounted on an IX71 inverted microscope (Olympus) equipped with a 60x oil objective (UPlanSApo, NA 1.35, Olympus) or 40x silicone objective (UPlanSApo, NA 1.25, Olympus). Images were acquired with an sCMOS camera (Prime 95B, Teledyne Imaging, Tucson, Az, USA) controlled by μManager (Edelstein et al., 2014). GFP and mCherry were excited with a 488nm and a 561nm laser, respectively. The exposure time was set such that the signal intensity was not saturated at any position.

F-actin staining and immunostaining for p-MLC

C. elegans embryos were fixed after removing the eggshell. For phalloidin staining, the embryos were fixed for 30 minutes at room temperature in a solution containing 2% PFA, 0.25% Glutaraldehyde, HEPES (pH6.9) 100mM, EGTA (pH7.0) 50mM, $MgSO_4$ 10mM, Triton X-100 0.2%, Dextrose 100mM after the eggshell removal. The buffer composition followed previous publications (Munro et al., 2004; Sugioka and Bowerman, 2018). After fixation, the embryos were washed in PBS three times, and then incubated with Phalloidin Alexa568 (Thermo Fisher scientific) for two hours at room temperature.

For immunostaining, the eggshell was removed from the embryos and these were fixed in 4% PFA, HEPES (pH6.9) 100mM, EGTA (pH7.0) 50mM, $MgSO_4$ 10mM, Triton X-100 0.2%, Dextrose 100mM for 30 minutes at room temperature. The embryos were then washed with 0.1% Triton in PBS three times. They were then incubated with a rabbit anti-phosphomyosin S19 antibody (1:200 dilution, #3671, Cell signaling technology, Danvers, Ma, USA) diluted in PBS with horse serum and 0.01% Triton at 4C overnight. The fixed embryos were then washed with PBS three times. They were then incubated with goat anti-Rabbit Alexa568 in PBS at room temperature for two hours. The embryos were then washed with PBS three times.

The embryos were then placed on a coverslip coated with Poly-lysine to bind them to the surface. Images were acquired using a FV1200 laser scanning confocal head mounted on an IX83 microscope equipped with GASp detectors (Olympus). Optical sections were acquired at 0.25µm intervals along the z-axis.

Image analysis

1. Angle measurement

Images were semi-automatically segmented based on membrane fluorescence signal from PH-PLδ-GFP. Cell contours were obtained by thresholding of the intensity, and processed using a custom mesh generation pipeline based on distance transforms and Delaunay-Triangulation to generate a triangular tilling of the images and line contour segmentation based on the triangles of the tilling. Our method returns the borders of the cells as multi-material polygonal line, that can be used to extract all the junctional angles (see **Supplemental Theory**). We confirmed that angle measurement was not affected by small offsets in the plane of imaging from the embryo midplane (**Fig S1C,D**).

2. Fluorescent intensity measurement

In order to measure average value of the fluorescent intensity along different parts of the cell contour, images were semi-automatically segmented using a Fiji plugin, TissueAnalyzer (Aigouy et al., 2016). The segmented images were subdivided into cortical regions and intercellular adhesions. Regions were then dilated to increase their width. Those regions were used to define ROI to obtain pixel values contained within each region. A MATLAB script was written to collect extract pixel values and calculate a mean intensity for each ROI.

Statistical analysis

To confirm normality, the Shapiro–Wilk test was used. To confirm homoscedasticity, an F-test was used. If both normality and homoscedasticity were confirmed, Student's t-test was used to compare means; In other cases, Wilcoxon's rank sum test was used to compare median values. $P<0.05$ was considered to represent statistical significance. For these analyses, R (www.r-project.org) or MATLAB was used.

Myosin-informed tension inference

We first infer ratios of surface tensions from angle measurements by solving a linear system of modified Young-Dupré equations, complemented by a constraint of mean tension equal to unity (see details in the **Supplemental theory**). Then we fix the scales of the tensions in space and in time using the evolution of myosin intensity values at the interface between P2 and the external medium. Finally, the regression between myosin intensity and tension values measured by AFM allows us to create

spatiotemporal maps of absolute values of surface tensions within the embryo.

Active foam 3D simulations and 2D numerical sections

Knowing cells volumes and relative surface tensions (through inference), we can minimize the surface energy $E = \sum_{\{ij\}} A_{ij}\gamma_{ij}$ (where A_{ij} stands for the interface between regions i,j) under the constraints of conservation of the volume of each individual cell. We start from an initial triangular mesh with a topology similar to the corresponding wild-type embryo at the same stage. Using a conjugate-gradient numerical scheme to optimize the energy and a projection method to implement volume conservation constraints (see **Supplemental theory**), the mesh is evolved until a convergence criterium is reached, while remeshing operations are performed during optimization when necessary (when a topology change may occur for instance, or when the mesh is too distorted). A penalization energy (see **Supplemental theory**) is added to mimic the confinement within the shell (**Supplemental theory Fig 5**), whose shape is approximated to a prolate ellipsoid of dimensions given in **Supplemental theory Fig 4**. To mimic optical sectioning, we intersect the triangular mesh with a plane and we determine polygonal line contours of cells in the corresponding focal plane using the CGal library (https://www.cgal.org, see **Supplemental theory Fig 6**). Interface lengths can be easily calculated on this polygonal 2D representation of cells interface contours and compared to those obtained from segmentation meshes.

Data availability

Primary data is available from the UCL data repository (https://rdr.ucl.ac.uk/) with a unique doi (10.5522/04/21977771).

Segmentation and force inference software are available on the following repository:
https://github.com/VirtualEmbryo/foambryo2D

Supplemental videos

Video S1. Measurement of cortical tension dynamics using AFM, related to Figure 2. The AFM cantilever was left in contact with the cell for the duration of its cell cycle.

Video S2. Time-lapse movie of a developing *C. elegans* embryo expressing a GFP-tagged membrane marker and mCherry-tagged histone marker. Embryos were without eggshell and observed from 1-cell to 2-cell stage, related to Figure S1, S3 (left), and from 2-cell to 4-cell stage, related to Figures 3, S1 (right). Scale bar = 10μm.

Video S3. Movies of 3D active foam simulations of the *C. elegans* embryo without an eggshell at the 2-cell stage (left) and 4-cell stage (right), related to Figures 3, S3.

Video S4. Time-lapse movie of a developing *C. elegans* embryo expressing a GFP-tagged membrane marker and mCherry-tagged histone marker within the eggshell. Embryos were observed from 1-cell to 8-cell stage, related to Figure 5, S1, S3 (left). *C. elegans* embryo expressing a GFP fusion to the endogenous NMY-2 gene within the eggshell from 1-cell to 8-cell stage, related to Figures 4, S4 (right). Scale bar = 10μm.

Video S5. Movies of 3D active foam simulations of the *C. elegans* embryo within the eggshell at the 2-cell stage (left) and 4-cell stage (right), related to Figures 5, S3.

Video S6. Time-lapse movie of a developing *C. elegans* embryo expressing a GFP fusion to the endogenous HMR-1 gene within the eggshell from 1-cell to 8-cell stage, related to Figures 7, S5. Scale bar = 10μm.

References

Aigouy, B., Umetsu, D., and Eaton, S. (2016). Segmentation and Quantitative Analysis of Epithelial Tissues. Methods Mol Biol *1478*, 227-239.

Bambardekar, K., Clement, R., Blanc, O., Chardes, C., and Lenne, P.F. (2015). Direct laser manipulation reveals the mechanics of cell contacts in vivo. Proc Natl Acad Sci U S A *112*, 1416-1421.

Barriga, E.H., Franze, K., Charras, G., and Mayor, R. (2018). Tissue stiffening coordinates morphogenesis by triggering collective cell migration in vivo. Nature *554*, 523-527.

Behrndt, M., Salbreux, G., Campinho, P., Hauschild, R., Oswald, F., Roensch, J., Grill, S.W., and Heisenberg, C.P. (2012). Forces driving epithelial spreading in zebrafish gastrulation. Science *338*, 257-260.

Brenner, S. (1974). The genetics of Caenorhabditis elegans. Genetics *77*, 71-94.

Brodland, G.W., Conte, V., Cranston, P.G., Veldhuis, J., Narasimhan, S., Hutson, M.S., Jacinto, A., Ulrich, F., Baum, B., and Miodownik, M. (2010). Video force microscopy reveals the mechanics of ventral furrow invagination in Drosophila. Proc Natl Acad Sci U S A *107*, 22111-22116.

Chan, E.H., Chavadimane Shivakumar, P., Clement, R., Laugier, E., and Lenne, P.F. (2017). Patterned cortical tension mediated by N-cadherin controls cell geometric order in the

Drosophila eye. Elife *6*.

Chugh, P., Clark, A.G., Smith, M.B., Cassani, D.A.D., Dierkes, K., Ragab, A., Roux, P.P., Charras, G., Salbreux, G., and Paluch, E.K. (2017). Actin cortex architecture regulates cell surface tension. Nat Cell Biol *19*, 689-697.

Collinet, C., Rauzi, M., Lenne, P.F., and Lecuit, T. (2015). Local and tissue-scale forces drive oriented junction growth during tissue extension. Nat Cell Biol *17*, 1247-1258.

David, R., Luu, O., Damm, E.W., Wen, J.W., Nagel, M., and Winklbauer, R. (2014). Tissue cohesion and the mechanics of cell rearrangement. Development *141*, 3672-3682.

Edelstein, A.D., Tsuchida, M.A., Amodaj, N., Pinkard, H., Vale, R.D., and Stuurman, N. (2014). Advanced methods of microscope control using muManager software. J Biol Methods *1*.

Fickentscher, R., Krauss, S.W., and Weiss, M. (2018). Anti-correlation of cell volumes and cell-cycle times during the embryogenesis of a simple model organism. New J Phys *20*.

Firmin, J., Ecker, N., Rivet Danon, D., Barraud Lange, V., Turlier, H., Patrat, C., and Maitre, J.L. (2022). Mechanics of human embryo compaction. BiorXiv.

Firmino, J., Rocancourt, D., Saadaoui, M., Moreau, C., and Gros, J. (2016). Cell Division Drives Epithelial Cell Rearrangements during Gastrulation in Chick. Dev Cell *36*, 249-261.

Fischer-Friedrich, E., Hyman, A.A., Julicher, F., Muller, D.J., and Helenius, J. (2014). Quantification of surface tension and internal pressure generated by single mitotic cells. Sci Rep *4*, 6213.

Fraser, A.G., Kamath, R.S., Zipperlen, P., Martinez-Campos, M., Sohrmann, M., and Ahringer, J. (2000). Functional genomic analysis of C. elegans chromosome I by systematic RNA interference. Nature *408*, 325-330.

Godard, B.G., Dumollard, R., Munro, E., Chenevert, J., Hebras, C., McDougall, A., and Heisenberg, C.P. (2020). Apical Relaxation during Mitotic Rounding Promotes Tension-Oriented Cell Division. Dev Cell *55*, 695-706 e694.

Guevorkian, K., and Maitre, J.L. (2017). Micropipette aspiration: A unique tool for exploring cell and tissue mechanics in vivo. Methods Cell Biol *139*, 187-201.

Hayashi, T., and Carthew, R.W. (2004). Surface mechanics mediate pattern formation in the developing retina. Nature *431*, 647-652.

Kale, G.R., Yang, X., Philippe, J.M., Mani, M., Lenne, P.F., and Lecuit, T. (2018). Distinct contributions of tensile and shear stress on E-cadherin levels during morphogenesis. Nat Commun *9*, 5021.

Kamath, R.S., Martinez-Campos, M., Zipperlen, P., Fraser, A.G., and Ahringer, J. (2001).

Effectiveness of specific RNA-mediated interference through ingested double-stranded RNA in Caenorhabditis elegans. Genome Biol *2*, RESEARCH0002.

Maitre, J.L., Berthoumieux, H., Krens, S.F., Salbreux, G., Julicher, F., Paluch, E., and Heisenberg, C.P. (2012). Adhesion functions in cell sorting by mechanically coupling the cortices of adhering cells. Science *338*, 253-256.

Maitre, J.L., Niwayama, R., Turlier, H., Nedelec, F., and Hiiragi, T. (2015). Pulsatile cell-autonomous contractility drives compaction in the mouse embryo. Nat Cell Biol *17*, 849-855.

Maitre, J.L., Turlier, H., Illukkumbura, R., Eismann, B., Niwayama, R., Nedelec, F., and Hiiragi, T. (2016). Asymmetric division of contractile domains couples cell positioning and fate specification. Nature *536*, 344-348.

Mayer, M., Depken, M., Bois, J.S., Julicher, F., and Grill, S.W. (2010). Anisotropies in cortical tension reveal the physical basis of polarizing cortical flows. Nature *467*, 617-621.

Mickey, K.M., Mello, C.C., Montgomery, M.K., Fire, A., and Priess, J.R. (1996). An inductive interaction in 4-cell stage C. elegans embryos involves APX-1 expression in the signalling cell. Development *122*, 1791-1798.

Mitchison, J.M., and Swann, M.M. (1954). The Mechanical Properties of the Cell Surface .1. The Cell Elastimeter. J Exp Biol *31*, 443-&.

Munro, E., Nance, J., and Priess, J.R. (2004). Cortical flows powered by asymmetrical contraction transport PAR proteins to establish and maintain anterior-posterior polarity in the early C. elegans embryo. Dev Cell *7*, 413-424.

Munro, E.M., and Odell, G.M. (2002). Polarized basolateral cell motility underlies invagination and convergent extension of the ascidian notochord. Development *129*, 13-24.

Noll, N., Streichan, S.J., and Shraiman, B.I. (2020). A variational method for image-based inference of internal stress in epithelial tissues. Phys Rev X *10*.

Norotte, C., Marga, F., Neagu, A., Kosztin, I., and Forgacs, G. (2008). Experimental evaluation of apparent tissue surface tension based on the exact solution of the Laplace equation. Epl-Europhys Lett *81*.

Padmanabhan, A., Ong, H.T., and Zaidel-Bar, R. (2017). Non-junctional E-Cadherin Clusters Regulate the Actomyosin Cortex in the C. elegans Zygote. Curr Biol *27*, 103-112.

Park, F.D., and Priess, J.R. (2003). Establishment of POP-1 asymmetry in early C. elegans embryos. Development *130*, 3547-3556.

Prevedel, R., Diz-Munoz, A., Ruocco, G., and Antonacci, G. (2019). Brillouin microscopy: an emerging tool for mechanobiology. Nat Methods *16*, 969-977.

Rauzi, M., Verant, P., Lecuit, T., and Lenne, P.F. (2008). Nature and anisotropy of cortical

forces orienting Drosophila tissue morphogenesis. Nat Cell Biol *10*, 1401-1410.

Rocheleau, C.E., Downs, W.D., Lin, R., Wittmann, C., Bei, Y., Cha, Y.H., Ali, M., Priess, J.R., and Mello, C.C. (1997). Wnt signaling and an APC-related gene specify endoderm in early C. elegans embryos. Cell *90*, 707-716.

Roffay, C., Chan, C.J., Guirao, B., Hiiragi, T., and Graner, F. (2021). Inferring cell junction tension and pressure from cell geometry. Development *148*.

Salbreux, G., Charras, G., and Paluch, E. (2012). Actin cortex mechanics and cellular morphogenesis. Trends Cell Biol *22*, 536-545.

Serwane, F., Mongera, A., Rowghanian, P., Kealhofer, D.A., Lucio, A.A., Hockenbery, Z.M., and Campas, O. (2017). In vivo quantification of spatially varying mechanical properties in developing tissues. Nat Methods *14*, 181-186.

Shelton, C.A., and Bowerman, B. (1996). Time-dependent responses to glp-1-mediated inductions in early C. elegans embryos. Development *122*, 2043-2050.

Sherrard, K., Robin, F., Lemaire, P., and Munro, E. (2010). Sequential activation of apical and basolateral contractility drives ascidian endoderm invagination. Curr Biol *20*, 1499-1510.

Singh, D., and Pohl, C. (2014). Coupling of rotational cortical flow, asymmetric midbody positioning, and spindle rotation mediates dorsoventral axis formation in C. elegans. Dev Cell

28, 253-267.

Sonnichsen, B., Koski, L.B., Walsh, A., Marschall, P., Neumann, B., Brehm, M., Alleaume, A.M., Artelt, J., Bettencourt, P., Cassin, E.*, et al.* (2005). Full-genome RNAi profiling of early embryogenesis in Caenorhabditis elegans. Nature *434*, 462-469.

Stewart, M.P., Helenius, J., Toyoda, Y., Ramanathan, S.P., Muller, D.J., and Hyman, A.A. (2011). Hydrostatic pressure and the actomyosin cortex drive mitotic cell rounding. Nature *469*, 226-230.

Stiernagle, T. (2006). Maintenance of C. elegans. WormBook, 1-11.

Sugioka, K., and Bowerman, B. (2018). Combinatorial Contact Cues Specify Cell Division Orientation by Directing Cortical Myosin Flows. Dev Cell *46*, 257-270 e255.

Tada, M., and Kai, M. (2012). Planar cell polarity in coordinated and directed movements. Curr Top Dev Biol *101*, 77-110.

Thompson, C.J., Vu, V.H., Leckband, D.E., and Schwartz, D.K. (2021). Cadherin cis and trans interactions are mutually cooperative. Proc Natl Acad Sci U S A *118*.

Thorpe, C.J., Schlesinger, A., Carter, J.C., and Bowerman, B. (1997). Wnt signaling polarizes an early C. elegans blastomere to distinguish endoderm from mesoderm. Cell *90*, 695-705.

Turlier, H., and Maitre, J.L. (2015). Mechanics of tissue compaction. Semin Cell Dev Biol *47*-

48, 110-117.

Voiculescu, O., Bertocchini, F., Wolpert, L., Keller, R.E., and Stern, C.D. (2007). The amniote primitive streak is defined by epithelial cell intercalation before gastrulation. Nature *449*, 1049-1052.

Yamamoto, K., and Kimura, A. (2017). An asymmetric attraction model for the diversity and robustness of cell arrangement in nematodes. Development *144*, 4437-4449.

Yu, H.H., Dohn, M.R., Markham, N.O., Coffey, R.J., and Reynolds, A.B. (2016). p120-catenin controls contractility along the vertical axis of epithelial lateral membranes. J Cell Sci *129*, 80-94.

Zhu, M., and Zernicka-Goetz, M. (2020). Building an apical domain in the early mouse embryo: Lessons, challenges and perspectives. Curr Opin Cell Biol *62*, 144-149.

Supplemental theory

Dissecting the subcellular forces sculpting early *C. elegans* embryos

Kazunori Yamamoto[1,2*], Sacha Ichbiah[3*], Joana Pinto[4], Fabrice Delbary[3], Nate Goehring[4], Hervé Turlier[3†], Guillaume Charras[1,5,6†]

[1] London Centre for Nanotechnology, University College London, 17-19 Gordon Street, London WC1H 0AH, UK
[2] Applied Bioscience, Kanagawa Institute of Technology, 1030 Shimo-Ogino Atsugi Kanagawa, 243-0203, Japan
[3] Center for Interdisciplinary Research in Biology (CIRB), Collège de France, CNRS, INSERM, Université PSL, 11, place Marcelin Berthelot, Paris, 75005, France.
[4] The Francis Crick institute, London NW1 1AT, UK
[5] Department of Cell and Developmental Biology, University College London, Gower Street, London WC1E 6BT, UK
[6] Institute for the Physics of Living Systems, University College London, Gower Street, London WC1E 6BT, UK

* These authors contributed equally to this work
† Corresponding authors: herve.turlier@college-de-france.fr, g.charras@ucl.ac.uk

1 Cell tension measurement with AFM

In the next, we assume that the cell-medium tension of *C. elegans* blastomeres is homogeneous and isotropic and that a quasistatic equilibrium has been reached. The latter hypothesis is well justified by the rapid relaxation of the force ($\lesssim 30s$) after compression by an AFM cantilever, as shown on Fig S1E.

We detail below the main equations used to calculate the cell-medium surface tension γ using the measured the force F and height h measured by AFM and optical measurements of the cell radius r_1 in the midplane, as depicted on the schematics below:

The compressed cell of height h has rotational symmetry with respect to the $(0z)$ axis and plane symmetry with respect to (Oxy). Its profile is parameterised as $r \mapsto z(r)$, and r_1, r_2 are the principal radii of curvature at the midplane, r_3 is the contact radius between the AFM cantilever and the cell with θ the contact angle. The cell surface tension is denoted γ, the AFM force F and the pressure difference across the cell membrane $\Delta P \equiv P_i - P_o$.

General case

Our derivation follows [1] and starts from Laplace's equation, which expresses normal force balance along the free cell profile

$$\Delta P = \text{constant} = \gamma\Big(C_1(r,z) + C_2(r,z)\Big) = \gamma\left[\frac{z'}{r(1+z'^2)^{1/2}} + \frac{z"}{(1+z'^2)^{3/2}}\right], \tag{1}$$

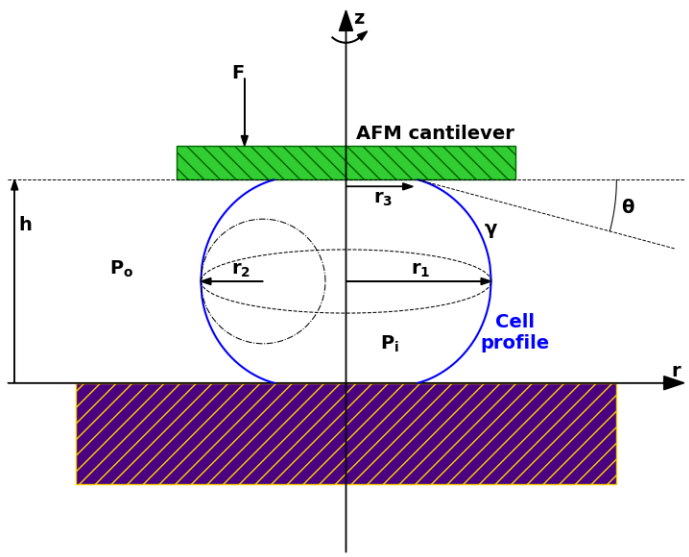

Figure 1: Scheme of surface tension measurements using an AFM cantilever

where $z' = \frac{dz}{dr}$, $z" = \frac{d^2z}{dr2}$ and $C_1(r,z)$ and $C_2(r,z)$ are the two local principal curvatures at each point r, z belonging to the cell profile. The cell pressure is homogeneous and constant from the assumption of a quasistatic equilibrium (no cytoplasmic flow or tension change).

Integration of this equation along the profile between $r = r_1$ (midplane) and $r \leq r_3$ yields

$$z'(x) = \left[\left(\frac{x}{\alpha x^2 - \alpha + 1}\right)^2 - 1\right]^{-1/2} \tag{2}$$

where we have defined a dimensionless parameter $\alpha = \dfrac{r_1 \Delta P}{2\gamma}$ and introduced a normalized radius $x \equiv r/r_1$. Note that this profile is not a circular arc, but enters the category of onduloids. Integration of the derivative of the normalized profile $z'(x)$ between the midplane $x = 1$ and the cell-AFM contact $x = r_3/r_1 \equiv \beta_\theta(\alpha)$ gives half the height $h/2$ normalized by r_1

$$\frac{h}{2r_1} = f_\theta(\alpha), \quad \text{where} \quad f_\theta(\alpha) = \int_{\beta_\theta(\alpha)}^{1} z'(x)\, dx, \tag{3}$$

This equation therefore relates h, r_1, α and θ (via the function $\beta_\theta(\alpha)$)

The force exerted by the AFM cantilever can be expressed along the z-axis at the cell-cantilever contact surface as a function of r_3 and θ

$$F = \Delta P \pi r_3^2 - 2\pi r_3 \gamma \sin\theta, \tag{4}$$

which leads to a 2nd-order equation for $y \equiv r_3/r_1 = \beta_\theta(\alpha)$ by equating to the previous expression (7) $\alpha y^2 - y \sin\theta + (1 - \alpha) = 0$. The only physically meaningful solution of this equation is

$$y = \frac{\sin\theta + \sqrt{\sin^2\theta + 4\alpha(\alpha - 1)}}{2\alpha} = \beta_\theta(\alpha) \tag{5}$$

This equation therefore gives an explicit formula for $\beta_\theta(\alpha)$.

Finally, we can also express the force balance along the z-axis at the midplane to relate the measured force F to the cell tension γ and to the pressure difference ΔP

$$F = \Delta P \pi r_1^2 - 2\pi r_1 \gamma. \tag{6}$$

From Laplace's equation (1) expressed at the midplane $\Delta P = \gamma \left(\frac{1}{r_1} + \frac{1}{r_2} \right)$ we deduce $r_2 = \frac{r_1}{2\alpha - 1}$. and by replacing in the equation (6) above yields

$$F = 2\pi\gamma r_1(\alpha - 1). \tag{7}$$

This equation relates F, r_1, γ and α.

Hence, with h, r_1 and θ measured, we can solve the non-linear equation (3) to get α, then the surface tension γ can be expressed using this solution and the measured radius r_1 and the measured force F using (7) as

$$\gamma = \frac{F}{2\pi r_1(\alpha - 1)}. \tag{8}$$

Note that the cells do not adhere to the AFM cantilever or the coverslip, so in our calculations we assume that the contact angle $\theta \sim 0$.

2 Image segmentation

To perform tension inference from microscopy images of the embryos and to validate our method, we need to extract precise geometrical features from the images: the contact angles at tricellular junctions and the length of all the cellular interfaces. Several libraries, such as *cellpose* [13], exist to segment microscopy images of cells into binary cell masks. Extracting geometrical features from pixel-based cell masks remains however inconvenient and imprecise.

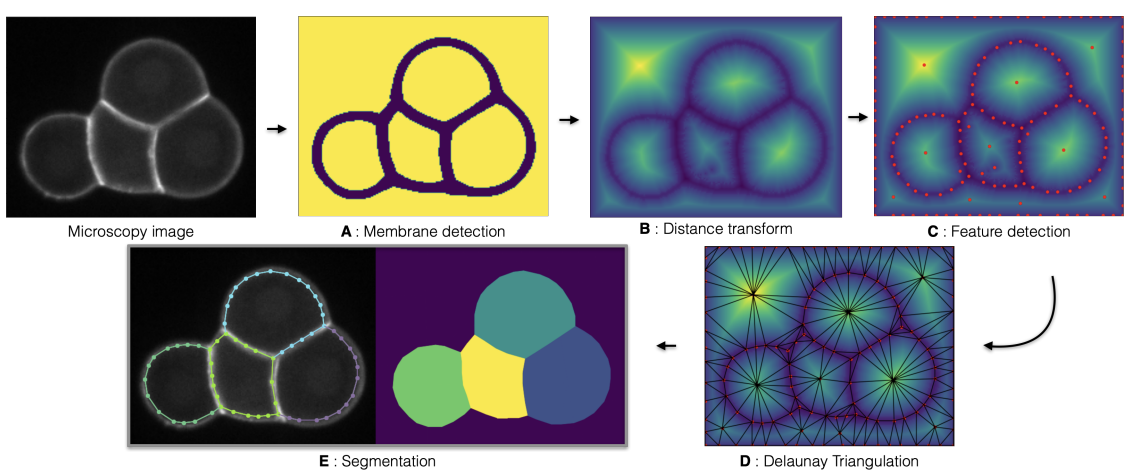

Figure 2: Delaunay-Watershed mesh segmentation pipeline. **A.** The membrane is segmented using a simple thresholding **B.** A topological map is created from the membrane contour by computing the euclidean distance transform. **C.** Feature points are defined on the picture, consisting of all the local minima, the points of the border of the frame, and the local maxima. The local extrema are computed with a threshold distance based on the width of the membrane to diminish the number of points. **D.** The square grid is tessellated using Delaunay triangulation, giving us a description of the surface with a triangle based grid instead of the pixel based grid. **E.** The surface is segmented with a watershed algorithm, based on this new grid. The segmented instances (i.e cells) are described as the union of the triangles they contain (right). The borders of these instances are polygonal lines, that give a good description of the geometry of the membranes in 2D (left)

To avoid working on the initial pixel grid, we developed a specific segmentation pipeline, described in Fig 2. The main idea is to generate a polygonal line to describe cell contours, from which interface lengths and contact angles at tricellular junctions can be easily computed. The pipeline is decomposed into 5 steps:

1. From the microscopy images of cell membranes, we apply a thresholding operation to extract a rough mask of cell contours (marked as 1, while the exterior is 0), see Fig 2A.

2. From this mask, we calculate a Euclidean distance map: each pixel with a value 0 in the mask is replaced by its Euclidean distance to the closest pixel of value 1 or to the image borders, see Fig 2B.

3. The distance transform map creates a landscape of valleys and peaks, which are populated by seeding points based on user-defined lower and upper threshold values. Well-chosen thresholds lead to a sparse but precise enough contouring of cells and image borders, see Fig 2C.

4. From this set of points, we apply a Delaunay triangulation to mesh the image space, see Fig 2D.

5. To segment this triangular mesh, we consider instead the dual Voronoi graph $\mathcal{G} = (\mathcal{N}, \mathcal{L})$, where the nodes $\mathcal{N}$ are the triangles, and the links $\mathcal{L}$ are the edges of the triangles. This graph can be assigned weights by integrating the values of the Euclidean distance transform along the edges.

6. The nodes $\mathcal{N}$ of this weighted graph $\mathcal{G}$ can be grouped (clustered) together using a watershed algorithm, after giving it several seeds.

7. Eventually, the borders of the clusters can be extracted, giving polygonal lines that describe the geometry of the embryo.

The Euclidean distance transform and the Delaunay triangulation where done in Python using the library SciPy [6]. To implement the operations on the dual Voronoi graph, we used the library *NetworkX* [12].

With this pipeline, we have geometrically segmented all our images of the cell membranes of *C. elegans* embryos. To prove its usefulness for biologists, we tried it on other biological objects and compared it to the automated segmentation of [13]. Our Delaunay-Watershed pipeline is not as high-throughput as fully automated tools, mostly based on neural networks. We preferred to compromise on automation to gain in flexibility, offering users several parameters to fine-tune the segmentation (i.e the thresholding of the membrane and the density of anchor points), to obtain exactly the desired result. This tool allows us to more easily extract geometrical information (angles, lengths, curvatures) that is currently difficult to retrieve from traditional segmentation masks.

3 Tension inference

3.1 Derivation of the cotangent Young-Dupré formula

At a tricellular junction, three cell interfaces meet at angles $\theta_{k\in\{1,2,3\}}$. We can write the classical Young-Dupré tension balance as function of the tension amplitudes $\gamma_{ij\in\{1,2,3\}} = ||\vec{\gamma}_{ij\in\{1,2,3\}}||$:

$$0 = \gamma_{12} + \gamma_{23}\cos\theta_2 + \gamma_{31}\cos\theta_1 \tag{9}$$

$$0 = \gamma_{12}\cos\theta_2 + \gamma_{23} + \gamma_{31}\cos\theta_3 \tag{10}$$

$$0 = \gamma_{12}\cos\theta_1 + \gamma_{23}\cos\theta_3 + \gamma_{31} \tag{11}$$

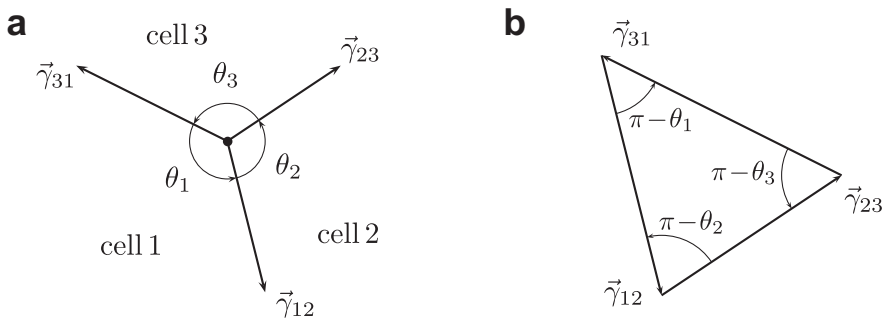

Figure 3: **Tensions equilibrium. a)** The three tensions $\vec{\gamma}_{ij\in\{1,2,3\}}$ tangent to interfacial contacts meet at a tricellular junction point with the contact angles $\theta_{k\in\{1,2,3\}}$. **b)** Tensions are at equilibrium when they form a triangle characterized by the internal angles $\pi-\theta_k$.

This set of equations is sufficient to infer accurately the tensions at each contact in the embryo without a shell. However, for embryos within a shell, our simulations parameterised with tensions inferred from this formula gave us less accurate results. We therefore looked for an alternative set of equations expressing the same force balance, but more that would be stable with respect to the typical values of contact angles that measured experimentally (often close to π).

For sake of simplicity, we denote by $z_{i,j,k} = \cot\left(\frac{\theta_{i,j,k}}{2}\right)$. The law of cotangents in the triangle formed by the three tensions gives for $i<j<k\in\{1,2,3\}$ can be written

$$z_k = \sqrt{\frac{(\gamma_{ij}+\gamma_{jk}-\gamma_{ki})(\gamma_{ij}+\gamma_{ki}-\gamma_{jk})}{(\gamma_{ij}+\gamma_{jk}+\gamma_{ki})(\gamma_{jk}+\gamma_{ki}-\gamma_{ij})}}.$$

Denoting by $t=\gamma_{ij}+\gamma_{jk}+\gamma_{ki}$ the perimeter of the triangle, we can rewrite the previous equations for $k\in\{1,2,3\}$ as

$$\gamma_{jk}+\gamma_{ki}-\gamma_{ij} = t z_i z_j,$$

That is

$$\begin{pmatrix} -1 & 1 & 1 \\ 1 & -1 & 1 \\ 1 & 1 & -1 \end{pmatrix} \begin{pmatrix} \gamma_{ij} \\ \gamma_{jk} \\ \gamma_{ki} \end{pmatrix} = t \begin{pmatrix} z_i z_j \\ z_j z_k \\ z_k z_i \end{pmatrix}$$

Hence

$$\begin{pmatrix} \gamma_{ij} \\ \gamma_{jk} \\ \gamma_{ki} \end{pmatrix} = \frac{t}{2} \begin{pmatrix} 0 & 1 & 1 \\ 1 & 0 & 1 \\ 1 & 1 & 0 \end{pmatrix} \begin{pmatrix} z_i z_j \\ z_j z_k \\ z_k z_i \end{pmatrix}$$

That is, for $i,j,k\in\{1,2,3\}$

$$\gamma_{ij} = \frac{t}{2}\cot\left(\frac{\theta_k}{2}\right)\left[\cot\left(\frac{\theta_i}{2}\right)+\cot\left(\frac{\theta_j}{2}\right)\right],$$

$$\gamma_{jk} = \frac{t}{2}\cot\left(\frac{\theta_i}{2}\right)\left[\cot\left(\frac{\theta_j}{2}\right)+\cot\left(\frac{\theta_k}{2}\right)\right],$$

$$\gamma_{ki} = \frac{t}{2}\cot\left(\frac{\theta_j}{2}\right)\left[\cot\left(\frac{\theta_k}{2}\right)+\cot\left(\frac{\theta_i}{2}\right)\right],$$

In the following, we name this set of equations the *cotangent Young-Dupré* formula.

We can thus compute the tensions of each junction from such equations directly from angle measurements, up to a multiplicative factor. We can eliminate this prefactor by computing ratios instead

$$\gamma_{ij} = \gamma_{jk} \frac{\cot(\frac{\theta_k}{2}) \left[\cot(\frac{\theta_i}{2}) + \cot(\frac{\theta_j}{2})\right]}{\cot(\frac{\theta_i}{2}) \left[\cot(\frac{\theta_j}{2}) + \cot(\frac{\theta_k}{2})\right]} \tag{12a}$$

$$\gamma_{jk} = \gamma_{ki} \frac{\cot(\frac{\theta_i}{2}) \left[\cot(\frac{\theta_k}{2}) + \cot(\frac{\theta_j}{2})\right]}{\cot\left(\frac{\theta_j}{2}\right) \left[\cot\left(\frac{\theta_k}{2}\right) + \cot\left(\frac{\theta_i}{2}\right)\right]} \tag{12b}$$

The tensions inferred from this linear set of equations are more stable, even when the contact angles approach π.

3.2 Numerical implementation of the tension inference problem

Each tricellular junction gives two independent *cotangent Young-Dupré equations* relating linearly interfacial tensions, as expressed above in equation (12). Considering all junctions in the embryo makes a set of equations $\mathcal{S}(\{\gamma_{ij}\}, \{\theta_i\}) = 0$, linear in γ_{ij}, that can be used to determine surface tensions from angle measurements. However, these equations only give ratios of surface tensions. To fix their scale, we arbitrarily set their mean to 1.

If we have n_j junctions and n_i interfaces, we can cast these equations in a matrix system

$$AX = B, \tag{13}$$

where we have defined $X = (\gamma_k)_{k=1}^{n_i}$ a vector collecting all the surface tensions, $A(\{\theta_i\}) \in \mathbb{R}^{(3n_j+1)\times n_i}$, a matrix implementing all the *cotangent Young-Dupré* equations (12) and the equation $\sum_{k=1}^{n_i} \gamma_k = n_i$ which constrains the mean tension to 1. This choice imposes the right hand side vector $B = (0, \ldots, 0, n_i) \in \mathbb{R}^{3n_j+1}$.

We want to determine X knowing $A(\{\theta_i\})$ and B. The matrix A is rectangular, but our problem is generically overdetermined because $n_j > n_i$. We choose to solve this problem using a pseudo-inverse and the Ordinary-Least-Squares (OLS) method that minimizes the sum of squared residuals, i.e that minimizes $\sum_{k=0}^{3n_j+1} ||(AX)_k - B_k||^2$. The solution can be expressed in a closed matrix form as

$$X = (A^T A)^{-1} A^T B \tag{14}$$

4 3D active-foam simulations

4.1 Model hypotheses

In our study, we assume that the shape of cells in the 2-cell and 4-cell *C. elegans* embryo is controlled primarily by surface tensions, in a similar manner as in other early embryos [2–4]. These surface tensions originate from contractility in the submembranous actomyosin cortex and are assumed to be homogeneous and isotropic at each cell interface. The tension of the plasma membrane is generically lower by an order of magnitude [3, 5] and the direct negative contribution of cadherin adhesion molecules is integrated in the surface tensions. An assembly of cells is therefore akin to a 3D foam, but where each interface may have a different surface tension, that is controlled actively by the cells sharing that interface. The evolution of cell shapes is assumed to be quasi-static, which means that viscous dissipation is neglected. Moreover, we assume that blastomeres conserve their volumes during the morphogenetic process.

A

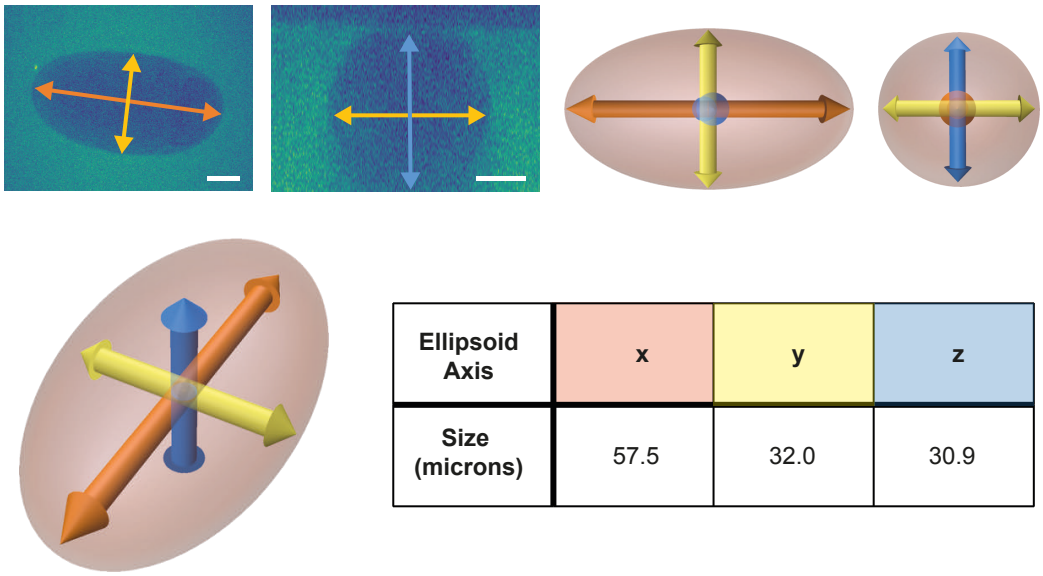

Ellipsoid Axis	x	y	z
Size (microns)	57.5	32.0	30.9

B

Cell name	AB	P1	ABa	ABp	EMS	P2
Volume (picoliters)	42.8	28.1	21.4	21.4	15.7	12.4

Figure 4: Measurement of the physical parameters for the simulation **A :** Shell axes are measured and used to determine the principal axes of an ellipsoid model of the shell. Scale bar : $10\mu m$ **B :** Table of cell volumes, in picoliters.

4.2 Determination of shell dimensions and cell volumes

We choose to model the shell as an ellipsoid. An ellipsoid may be defined by the equation

$$\frac{x^2}{l_x^2} + \frac{y^2}{l_y^2} + \frac{z^2}{l_z^2} = \frac{1}{4} \tag{15}$$

Where l_x, l_y, l_z are the length of the principal axes of the ellipsoid, respectively the orange, yellow, and blue arrows of figure 4A, that were measured experimentally.

For the cell volumes, we used the measurements of [9]. We note that the symmetric division of AB makes the volumes of ABa and ABp equal whereas the asymmetric division of P1 leads to different volumes for EMS and P2. For the embryo without the shell we keep the same volumes for all the cells, and the volumes of the daughter ABx cells are half the volume of the AB cell.

4.3 Lagrangian function and force on each vertex

Our numerical simulations consist in the minimisation of a surface energy under the constraint of cell volume conservation, where each interface is weighted by its surface tension. Simulations are performed on a non-manifold triangular mesh [10]. This formulation of the mechanical problem

is equivalent to Young-Laplace and Young-Dupré force balance equations for an isolated cell aggregate, as shown for a cell doublet in [4]. Here, we generalize this approach by implementing an additional constraint of non-penetration for the eggshell.

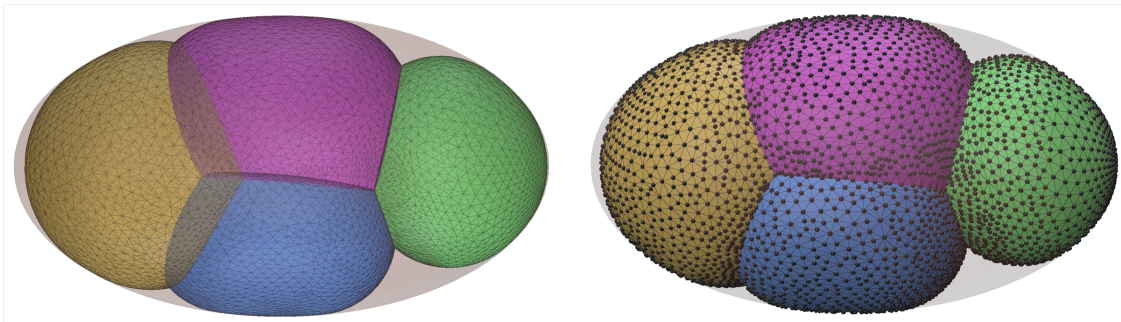

Figure 5: Multimaterial Mesh constrained to lie in an ellipsoidal shell (grey). (right) Vertices highlighted as dark dots. Each cell is coloured for ease of identification.

The surface energy for a set of N isolated cells is defined as follows

$$\mathcal{E} = \sum_{\text{pair } \{\text{lm}\} \in [\![0,\text{N}]\!]^2} \gamma_{lm} A_{lm}, \tag{16}$$

where γ_{lm} and A_{lm} are respectively the surface tension and the area of the interface between regions l and m, which span $[\![0, N]\!]$, with 0 referring to the external medium.

To add a constraint for the volume conservation of each cell, we define a Lagrangian function

$$\mathcal{L} = \mathcal{E} - \sum_{\text{cell l} \in [\![1,\text{N}]\!]} p_l \big(V_l - V_l^0\big), \tag{17}$$

where p_l, V_l and V_l^0 are respectively the pressure, the current volume and the target volume value of the cell l, which spans $[\![1, N]\!]$.

To model the confinement within the eggshell, we add to the energy $\mathcal{E}$ in (16) an additional elastic contribution $\mathcal{E}_{el}$ which is non-zero only for vertices that cross the eggshell boundary $\mathbf{x} > \mathcal{S}$

$$\mathcal{E}_{el} = \frac{K}{2} \sum_{\mathbf{x} > \mathcal{S}} ||\mathbf{x} - \mathbf{x}_{\mathcal{S}}(\mathbf{x})||^2, \tag{18}$$

where $\mathbf{x}_{\mathcal{S}}(\mathbf{x})$ is the orthogonal projection of the vertex $\mathbf{x}_t$ on the surface of the shell $\mathcal{S}$. A high value of K is chosen such that cell surfaces don't cross the eggshell by more than 0.1%.

From the Lagrangian function, one can calculate the force $\mathbf{f}_k$ on each vertex of the mesh $\mathbf{x} \in \{\mathbf{x}_k\}_{k=1}^n$ as follows

$$\mathbf{f} = -\frac{\partial \mathcal{L}}{\partial \mathbf{x}} \tag{19}$$

where $\mathbf{x} = x\mathbf{e}_x + y\mathbf{e}_y + z\mathbf{e}_z$ and $\mathbf{f} = f^x\mathbf{e}_x + f^y\mathbf{e}_y + f^z\mathbf{e}_z$ are the decomposition of vertex position and force in the 3D Euclidean space, equipped with an orthonormal basis $(\mathbf{e}_x, \mathbf{e}_y, \mathbf{e}_z)$.

Interfacial areas and cell volumes can be easily expressed as sums on the triangles t in the mesh:

$$A_{lm} = \sum_{t \in \{lm\}} a^t, \qquad V_l = \sum_{t \in \{l\}} v^t, \tag{20}$$

where $t \in \{lm\}$ means a triangle at the interface between a pair of regions of indices $0 \leq l \leq N$ and $0 \leq m \leq N$ and $t \in \{l\}$ means a triangle delimiting a cell of index $1 \leq l \leq N$. a^t and v^t are

respectively the elementary area and volume of a given triangle $t = \{\mathbf{x}_0^t, \mathbf{x}_1^t, \mathbf{x}_2^t\}$, which are given by

$$a^t = \frac{1}{2} \left| \left(\mathbf{x}_0^t - \mathbf{x}_2^t\right) \times \left(\mathbf{x}_1^t - \mathbf{x}_2^t\right) \right| \tag{21}$$

$$v^t = \frac{1}{6} \mathbf{x}_2^t \cdot \left(\mathbf{x}_0^t \times \mathbf{x}_1^t\right) \tag{22}$$

Their derivatives with respect to the vertex position $\mathbf{x} = \mathbf{x}_2^t$ may be easily calculated as

$$\frac{\partial a^t}{\partial \mathbf{x}} = \frac{1}{2} \left[\mathbf{n}^t \times \left(\mathbf{x}_1^t - \mathbf{x}_0^t\right)\right] \tag{23}$$

$$\frac{\partial v^t}{\partial \mathbf{x}} = \frac{1}{6} \mathbf{x}_0^t \times \mathbf{x}_1^t \tag{24}$$

where we have defined the normal $\mathbf{n}^t = (\mathbf{x}_0^t - \mathbf{x}_2^t) \times (\mathbf{x}_1^t - \mathbf{x}_0^t) / (2a^t)$ to the triangle t. Note that these formula are invariant by permutation of the triplet of vertices $\{0, 1, 2\}$.

The force on a vertex $\mathbf{x}$ defined in (19) may now be explicitly expressed as

$$\mathbf{f} = -\frac{\partial \mathcal{E}}{\partial \mathbf{x}} + \sum_{\text{cell l}} p_l \frac{\partial V_l}{\partial \mathbf{x}} \tag{25}$$

$$= -\sum_{\text{pair }\{\text{lm}\}} \frac{\gamma_{lm}}{2} \sum_{t \in \{lm\} | \mathbf{x} \in t} \mathbf{n}^t \times \left(\mathbf{x}_1^t - \mathbf{x}_0^t\right) + \sum_{\text{cell l}} p_l \sum_{t \in l | \mathbf{x} \in t} \frac{1}{6} \mathbf{x}_0^t \times \mathbf{x}_1^t \tag{26}$$

where we assumed without loss of generality that $\mathbf{x} = \mathbf{x}_2^t$, relying on the above invariance by permutation of derivatives formula.

The force on a vertex $\mathbf{x} > \mathcal{S}$ deriving from the additional shell elastic energy defined in equation (18) may be expressed as follows

$$\mathbf{f}_{el}(\mathbf{x}) = -K\left[\mathbf{x} - \mathbf{x}_{\mathcal{S}}(\mathbf{x})\right] \mathbf{N}_{\mathcal{S}}(\mathbf{x}_{\mathcal{S}}(\mathbf{x})) \tag{27}$$

where $\mathbf{N}_{\mathcal{S}}(\mathbf{x})$ is the normal of the surface of the shell at the point $\mathbf{x}$ (belonging to the shell), and $\mathbf{x}_{\mathcal{S}}(\mathbf{x})$ is the orthogonal projection of the vertex $\mathbf{x}$ on the surface of the shell $\mathcal{S}$.

4.4 Constrained optimization: projection method and conjugate gradient

To calculate the Lagrange multipliers $p_{l\,l=1}^{N}$, which enforce the volume conservation equations, we use a projection method [14].

The force $\mathbf{f}_k = \mathbf{f}\left(\mathbf{x}_k\right)$ of each vertex $\mathbf{x}_k$ in the mesh ($k \in [\![1, n]\!]$) is projected onto a subspace that is orthogonal to the space of cell volume variations

$$0 = \sum_{k=1}^{n} \mathbf{f}_k \cdot \frac{\partial V_l}{\partial \mathbf{x}_k} \qquad \forall l \in [\![1, N]\!] \tag{28}$$

This leads to a linear system of equations for p_l

$$\forall l \in [\![1, N]\!] \qquad \sum_{m=1}^{N} p_m \sum_{k=1}^{n} \left(\frac{\partial V_m}{\partial \mathbf{x}_k} \cdot \frac{\partial V_l}{\partial \mathbf{x}_k}\right) = \sum_{k=1}^{n} \left(\frac{\partial \mathcal{E}}{\partial \mathbf{x}_k} \cdot \frac{\partial V_l}{\partial \mathbf{x}_k}\right) \tag{29}$$

that may be rewritten in a condensed form $\underline{\underline{\boldsymbol{A}}} \cdot \mathbf{p} = \mathbf{b}$, where $\mathbf{p} \equiv \left(p_1, p_2, \ldots, p_N\right)$ is a vector of size N collecting the unknown pressures, $\mathbf{b} \equiv \left(\sum_k \left(\frac{\partial \mathcal{E}}{\partial \mathbf{x}_k} \cdot \frac{\partial V_1}{\partial \mathbf{x}_k}\right), \sum_k \left(\frac{\partial \mathcal{E}}{\partial \mathbf{x}_k} \cdot \frac{\partial V_2}{\partial \mathbf{x}_k}\right), \ldots, \sum_k \left(\frac{\partial \mathcal{E}}{\partial \mathbf{x}_k} \cdot \frac{\partial V_N}{\partial \mathbf{x}_k}\right)\right)$ is the vector of constants and $\underline{\underline{\boldsymbol{A}}}$ is the matrix of coefficients defined by

$$A_{lm} = \sum_k \left(\frac{\partial V_m}{\partial \mathbf{x}_k} \cdot \frac{\partial V_l}{\partial \mathbf{x}_k}\right) \qquad \forall l, m \in [\![1, N]\!] \tag{30}$$

which is a symmetric positive definite and therefore invertible matrix. This linear system of N equations is solved using Newton's method [7].

To find the mechanical equilibrium, one needs to solve the equation $\forall \mathbf{x}, \quad \mathbf{f}(\mathbf{x}) = 0$. To do so, we use an iterative method, namely the conjugate gradient, whereby the position $\mathbf{x}(t)$ of each vertex at time t is updated iteratively along a new search direction $\mathbf{D}_{t+1}$ that is conjugate to the one at previous time step $\mathbf{D}_t$ [7]. Here, we follow the Hestenes-Stiefel conjugate-gradient scheme [8]

$$\mathbf{D}_0 = -\frac{\partial \mathcal{L}}{\partial \mathbf{X}_0} = \mathbf{F}(\mathbf{X}_0) \tag{31a}$$

$$\mathbf{D}_{t+1} = \mathbf{F}(\mathbf{X}_0) + \beta_t^{\mathrm{HS}} \mathbf{D}_t \tag{31b}$$

$$\text{with} \quad \beta_t^{\mathrm{HS}} = \frac{\mathbf{F}(\mathbf{X}_{t+1}) \cdot \Big(\mathbf{F}(\mathbf{X}_{t+1}) - \mathbf{F}(\mathbf{X}_t)\Big)}{\mathbf{D}_t \cdot \Big(\mathbf{F}(\mathbf{X}_{t+1}) - \mathbf{F}(\mathbf{X}_t)\Big)}, \tag{31c}$$

where we have defined a generalized vertex position vector $\mathbf{X}_t = \Big(\mathbf{x}_1(t), \mathbf{x}_2(t), \ldots, \mathbf{x}_n(t)\Big)$ and a generalized force vector $\mathbf{F}(\mathbf{X}_t) = \Big(\mathbf{f}(\mathbf{x}_1(t)), \mathbf{f}(\mathbf{x}_2(t)), \ldots, \mathbf{f}(\mathbf{x}_n(t))\Big)$.

At each iteration, the cell pressures are recalculated using the projection method as described above.

The constrained optimization method is applied to a non-manifold multimaterial mesh following [10]. The identity of each interface separating cells i and j is tracked over its evolution by a label of integers (i, j) that is stored in each triangle of the interface. To maintain numerical precision, the triangular mesh is furthermore allowed to vary the number of vertices, edges and faces over its evolution (remeshing), and to perform topological transitions: T1 (neighbor exchange), T2 (region collapse) and merging (new contact). Note that, in contrast to classical vertex models where cell-cell boundaries are assumed to remain flat, our 3-dimensional model does not impose any prior constraints on cell shapes. Its precision in representing smooth and continuous interfaces is only limited by the user-defined resolution of the triangular mesh.

4.5 2D intersection of 3D simulation meshes of embryos

To compare the geometries of our 3D quasi-static simulations to experimentally acquired 2D microscopy images, we need compute the length of each interface defined in a plane intersecting the mesh. We used CGAL [11] to compute the intersection between our mesh and the midplane. This procedure gives directly the interfaces under the form of polygonal lines, from which we determine the length between all interfaces.

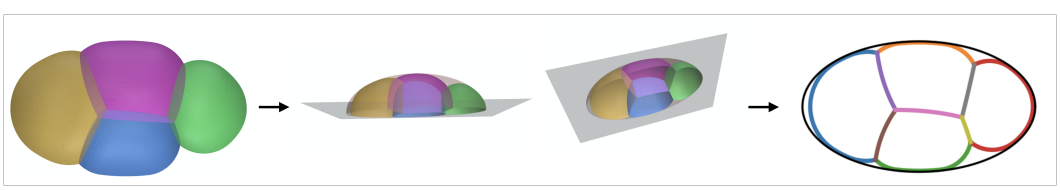

Figure 6: Geometrical extraction of the interfaces by computing the intersection of the focal plane and the 3D meshes

References

[1] Norotte, C., Marga, F., Neagu, A., Kosztin, I., & Forgacs, G. (2008). Experimental evaluation of apparent tissue surface tension based on the exact solution of the Laplace equation. EPL (Europhysics Letters), 81(4), 46003.

[2] Clark, A. G., Wartlick, O., Salbreux, G. & Paluch, E. K. Stresses at the Cell Surface during Animal Cell Review Morphogenesis. *Curr. Biol.* **24**, R484–R494 (2014).

[3] Maître, J. L., Niwayama, R., Turlier, H., Nédélec, F., & Hiiragi, T. Pulsatile cell-autonomous contractility drives compaction in the mouse embryo. *Nat. Cell Biol.* **17**, 849-855 (2015).

[4] Maître, J. L., Turlier, H., Illukkumbura, R., Eismann, B., Niwayama, R., Nédélec, F., & Hiiragi, T. Asymmetric division of contractile domains couples cell positioning and fate specification. *Nature* **536**, 344-348 (2016).

[5] Diz-Muñoz, A., Krieg, M., Bergert, M., Ibarlucea-Benitez, I., Muller, D. J., et al. Control of Directed Cell Migration In Vivo by Membrane-to-Cortex Attachment. *PLOS Biology* **8**, e1000544 (2010).

[6] Virtanen, P., Gommers, R., Oliphant, T. E., Haberland, M., Reddy, T., Cournapeau, D., ... Van Mulbregt, P. (2020). SciPy 1.0: fundamental algorithms for scientific computing in Python. *Nature methods*, **17**(3), 261-272.

[7] Nocedal, J., & Wright, S. *Numerical optimization.* (Springer Science & Business Media, 2006).

[8] Hestenes, M. R., & Stiefel, E. Methods of conjugate gradients for solving linear systems. *Washington, DC: NBS* **59** (1952).

[9] Fickentscher, R., Krauss, S. W., Weiss, M. (2018). Anti-correlation of cell volumes and cell-cycle times during the embryogenesis of a simple model organism. *New Journal of Physics*, **20**(11), 113001.

[10] Da, F., Batty, C., & Grinspun, E. Multimaterial mesh-based surface tracking. *ACM Trans. Graph.* **33**, 112:1-112:11 (2014).

[11] The CGal project. the Computational Geometry Algorithms Library. *https://www.cgal.org*

[12] Hagberg, A.A., Schult, D.A. & Swart, P.J. "Exploring network structure, dynamics, and function using NetworkX", in *Proceedings of the 7th Python in Science Conference (SciPy2008)*, Gäel Varoquaux, Travis Vaught, and Jarrod Millman (Eds), (Pasadena, CA USA), pp. 11–15, Aug 2008

[13] Stringer, C., Wang, T., Michaelos, M. et al. Cellpose: a generalist algorithm for cellular segmentation. *Nat. Methods* **18**, 100-1006 (2021).

[14] Brakke, K.A. Surface evolver manual. Mathematics Department, Susquehanna Univerisity, Selinsgrove, PA, vol. 17870, no 2.24, p. 20 (1994).